

Robust computation of dipole electromagnetic fields in arbitrarily anisotropic, planar-stratified environments

Kamalesh Sainath,^{1,*} Fernando L. Teixeira,^{1,†} and Burkay Donderici^{2,‡}

¹*ElectroScience Laboratory, The Ohio State University, 1330 Kinnear Road, Columbus, Ohio 43212, USA*

²*Halliburton, Sensor Physics and Technology, 3000 N. Sam Houston Pkwy E, Houston, Texas 77032, USA*

(Received 19 September 2013; published 31 January 2014)

We develop a general-purpose formulation, based on two-dimensional spectral integrals, for computing electromagnetic fields produced by arbitrarily oriented dipoles in planar-stratified environments, where each layer may exhibit arbitrary and independent anisotropy in both its (complex) permittivity and permeability tensors. Among the salient features of our formulation are (i) computation of eigenmodes (characteristic plane waves) supported in arbitrarily anisotropic media in a numerically robust fashion, (ii) implementation of an *hp*-adaptive refinement for the numerical integration to evaluate the radiation and weakly evanescent spectra contributions, and (iii) development of an adaptive extension of an integral convergence acceleration technique to compute the strongly evanescent spectrum contribution. While other semianalytic techniques exist to solve this problem, none have full applicability to media exhibiting arbitrary double anisotropies in each layer, where one must account for the whole range of possible phenomena (e.g., mode coupling at interfaces and nonreciprocal mode propagation). Brute-force numerical methods can tackle this problem but only at a much higher computational cost. The present formulation provides an efficient and robust technique for field computation in arbitrary planar-stratified environments. We demonstrate the formulation for a number of problems related to geophysical exploration.

DOI: [10.1103/PhysRevE.89.013312](https://doi.org/10.1103/PhysRevE.89.013312)

PACS number(s): 02.70.-c, 95.75.Pq

I. INTRODUCTION

The study of electromagnetic fields produced by dipole sources in planar-stratified environments with anisotropic layers is pertinent to many applications such as geophysical prospecting [1–7], microwave remote sensing [8], ground-penetrating radar [9,10], optical field focusing [11], antenna design [12,13], microwave circuits [14], and plasma physics [15]. For this problem class, one can exploit the planar symmetry and employ pseudoanalytical approaches based upon embedding spectral Green's function kernels within Fourier-type integrals to compute the space-domain fields [16–18]. A crucial aspect then becomes how to efficiently compute such integrals [19–23]. Based on the specific characteristics of the planar-stratified environment(s) considered, efficient, case-specific methods arise. For example, when one assumes isotropic layers so that no coupling between the TE_z and TM_z modes occurs at the planar interfaces, the original vector problem can be reduced to a set of scalar problems whose mixed domain Green's functions [i.e., those functions having (k_x, k_y, z) dependence] are either the primary kernels in integral representations of the Green's dyads (e.g., transmission-line-type Green's functions [17–19]) or the field components themselves (e.g., free-space Green's function [24]). Alternatively, when each layer exhibits azimuthal symmetry in its material properties, one can transform two-dimensional (2D), infinite-range Fourier integrals into one-dimensional, semi-infinite range Sommerfeld integrals [16–18,20–22]. For layers with arbitrary anisotropy, however, neither of the above simplifications apply, and a more general formulation is required.

Irrespective of the integral representation used, the following challenges exist concerning their numerical evaluation [19,24]: (i) The presence of branch points and branch cuts associated with semi-infinite and infinite-thickness layers, (ii) the presence of poles associated with slab- and interface-guided modes, and (iii) an oscillatory integrand that demands adequate sampling and whose exponential decay rate reduces with decreasing source-observer depth separation [21]. Among the approaches to address these issues one can cite direct numerical evaluation, possibly combined with integral acceleration techniques [19–22,25,26], asymptotic approximation of the space-domain field [24], and approximation of the mixed-domain integrand via a sum of analytically invertible images [19,23,27]. While image-approximation and asymptotic methods exhibit faster solution time, they are fundamentally approximate methods that either (respectively) require user intervention in performing *a priori* fine tuning, have medium-dependent applicability, and lack tight error-control [19,22], or have a limited range of applicability in terms of admitted medium classes and source and observer locations [24].

Since our focus is on the general applicability and robustness of the algorithm (and not on the optimality for a specific class of layer arrangements, medium parameters, and source-observer geometries), we adopt a direct numerical integration methodology based on 2D, infinite-range Fourier-type integrals. Some key ingredients of the present formulation are

(i) A numerically balanced recasting of the state matrix [24] to enable the accurate computation of the eigenmodes supported in media exhibiting arbitrary anisotropy (e.g., isotropic, uniaxial, biaxial, gyrotropic).

(ii) Closed-form eigenmode formulations for isotropic and reciprocal, electrically uniaxial media that significantly reduce eigenmode solution time (versus the state matrix method),

*sainath.1@osu.edu

†teixeira@ece.osu.edu

‡burkay.donderici@halliburton.com

obviate numerical overflow, and yield higher-precision results versus prior (canonical) formulations in Refs. [24,28].

(iii) A numerically stable method to decompose degenerate modes produced by sources in isotropic layers.

(iv) A multilevel, error-controlled, adaptive hp refinement procedure to evaluate the radiation and weakly evanescent spectral field contributions, employing nested Patterson-Gauss quadrature rules to reduce computation time.

(v) Adaptive extension of the original method of weighted averages (MWA) [20,26] and its application to accelerating the numerical evaluation of infinite-range, 2D Fourier-type integrals concerning environments containing media with arbitrary anisotropy and loss.

Section II overviews the formulation. Section III contains an analytical derivation of the mixed-domain, vector-valued integrand¹ $\mathbf{W}_L(k_x, k_y; z)$ of the 2D Fourier integral. Section IV exhibits an efficient numerical algorithm to compute the (inner) k_x integral in Eq. (2.13) (note that this discussion applies, in dual fashion, to the k_y integral).

II. FORMULATION OVERVIEW

Our problem concerns computing the electromagnetic field at $\mathbf{r} = (x, y, z)$ ² produced by a Herztian dipole source, which radiates at frequency ω within a planar-stratified, anisotropic environment at location $\mathbf{r}' = (x', y', z')$. We assume N layers stratified along the z axis as depicted in Fig. 1, each with (complex-valued) 3×3 material tensors³ $\bar{\epsilon}_c$ and $\bar{\mu}_c$ exhibiting independent and arbitrary anisotropy,⁴ that is⁵

$$\bar{\epsilon}_c = \epsilon_0 \bar{\epsilon}_r = \epsilon_0 \begin{bmatrix} \epsilon_{xx} & \epsilon_{xy} & \epsilon_{xz} \\ \epsilon_{yx} & \epsilon_{yy} & \epsilon_{yz} \\ \epsilon_{zx} & \epsilon_{zy} & \epsilon_{zz} \end{bmatrix}, \quad (2.1)$$

$$\bar{\mu}_c = \mu_0 \bar{\mu}_r = \mu_0 \begin{bmatrix} \mu_{xx} & \mu_{xy} & \mu_{xz} \\ \mu_{yx} & \mu_{yy} & \mu_{yz} \\ \mu_{zx} & \mu_{zy} & \mu_{zz} \end{bmatrix}$$

being simultaneous full, complex-valued tensors that can be different for each layer. With this in mind, Maxwell's equations in a homogeneous region with impressed electric and (equivalent) magnetic current densities⁶ \mathcal{J} and \mathcal{M} (respec-

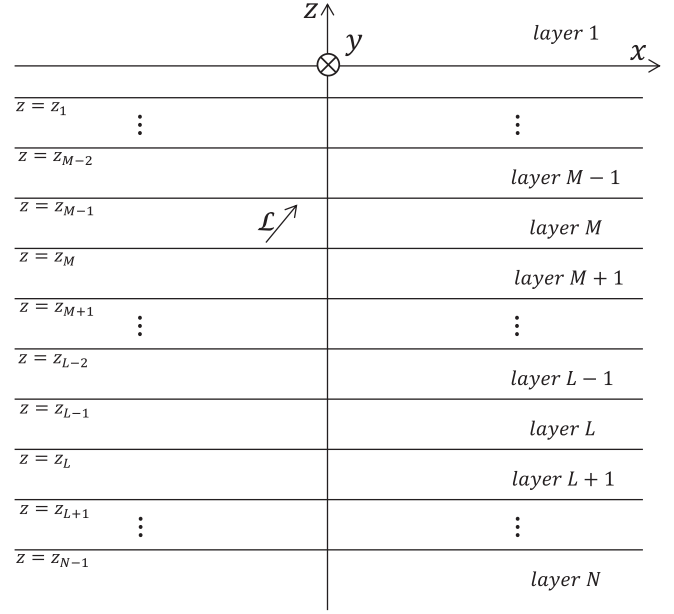


FIG. 1. Layer M contains the source point $\mathbf{r}' = (x', y', z')$ and layer L contains the observation point $\mathbf{r} = (x, y, z)$. The dipole source \mathcal{L} can be either electric or magnetic.

tively), as well as impressed volumetric electric and (equivalent) magnetic charge densities ρ_v and ρ_m (respectively), write as⁷

$$\nabla \times \mathcal{E} = i\omega \bar{\mu}_c \cdot \mathcal{H} - \mathcal{M} \quad (2.2)$$

$$\nabla \times \mathcal{H} = \mathcal{J} - i\omega \bar{\epsilon}_c \cdot \mathcal{E} \quad (2.3)$$

$$\nabla \cdot (\bar{\epsilon}_c \cdot \mathcal{E}) = \rho_v \quad (2.4)$$

$$\nabla \cdot (\bar{\mu}_c \cdot \mathcal{H}) = \rho_m. \quad (2.5)$$

After multiplying Eq. (2.2) by $\nabla \times \bar{\mu}_c^{-1} \cdot$ and using Eq. (2.3), one has [29]:

$$[\nabla \times (\bar{\mu}_c^{-1} \cdot \nabla \times) - \omega^2 \bar{\epsilon}_c \cdot] \mathcal{E} = i\omega \mathcal{J} - \nabla \times \bar{\mu}_c^{-1} \cdot \mathcal{M}. \quad (2.6)$$

Alternatively, defining the tensor-valued vector wave operator as

$$\bar{\mathcal{A}} = \nabla \times \bar{\mu}_r^{-1} \cdot \nabla \times - k_o^2 \bar{\epsilon}_r \quad (2.7)$$

one can reexpress Eq. (2.6) as

$$\bar{\mathcal{A}} \cdot \mathcal{E} = ik_o \eta_o \mathcal{J} - \nabla \times \bar{\mu}_r^{-1} \cdot \mathcal{M}, \quad (2.8)$$

where $k_o = \omega \sqrt{\epsilon_o \mu_o}$ (m^{-1}) and $\eta_o = \sqrt{\mu_o / \epsilon_o}$ (Ω) are the wave number and wave impedance of free space (respectively).

¹Vector, matrix, and tensor quantities have boldface script. Furthermore, field quantities with (k_x, k_y, z) dependence are denoted mixed-domain quantities.

²Note: z can refer to the observation depth or the coordinate, depending on context.

³Matrix and tensor quantities are denoted by an over-bar.

⁴We assume the material tensors to be diagonalizable, as this facilitates using plane wave fields as a basis to synthesize the field solution. Since all naturally occurring media possess diagonalizable material tensors, this constraint is not a practical concern and thus warrants no further discussion.

⁵ c_o (m/s) is the speed of light in free space, μ_o (H/m) is the free space magnetic permeability, and $\epsilon_o = \frac{1}{\mu_o c_o^2}$ (F/m) is the free space electric permittivity.

⁶Field quantities exhibiting purely spatial dependence have calligraphic script and are denoted spatial quantities.

⁷ i is the unit-magnitude imaginary number, $\omega = 2\pi f$ (rad/sec) is the angular frequency at which the source radiates, and the time convention $\exp(-i\omega t)$ is assumed and suppressed.

Now, define a three-dimensional Fourier Transform (FT) pair as⁸:

$$\tilde{\mathbf{E}}(\mathbf{k}) = \iiint_{-\infty}^{+\infty} \mathcal{E}(\mathbf{r}) e^{-i\mathbf{k}\cdot\mathbf{r}} dx dy dz, \quad (2.9)$$

$$\mathcal{E}(\mathbf{r}) = \left(\frac{1}{2\pi}\right)^3 \iiint_{-\infty}^{+\infty} \tilde{\mathbf{E}}(\mathbf{k}) e^{i\mathbf{k}\cdot\mathbf{r}} dk_x dk_y dk_z \quad (2.10)$$

with $\mathbf{r} = (x, y, z)$ and $\mathbf{k} = (k_x, k_y, k_z)$, and similarly for all other field and source quantities. Now, assuming an electric or magnetic dipole source (respectively), one has⁹ $\mathcal{J} = \hat{\mathbf{a}}J_o\delta(\mathbf{r}-\mathbf{r}')$ or $\mathcal{M} = \hat{\mathbf{a}}M_o\delta(\mathbf{r}-\mathbf{r}')$ in the space domain and $\tilde{\mathbf{J}} = \hat{\mathbf{a}}J_o$ or $\tilde{\mathbf{M}} = \hat{\mathbf{a}}M_o$ in the Fourier domain. To determine the spectral-domain fields, we first write the inverse of $\tilde{\mathbf{A}}$ as $\text{inv}(\tilde{\mathbf{A}}) = \text{adj}(\tilde{\mathbf{A}})/\det(\tilde{\mathbf{A}})$, where $\text{adj}(\tilde{\mathbf{A}})$ is the adjugate matrix (*not* the conjugate-transpose matrix) [30]. The determinant $\det(\tilde{\mathbf{A}}) = g_o(k_z - \tilde{k}_{1z})(k_z - \tilde{k}_{2z})(k_z - \tilde{k}_{3z})(k_z - \tilde{k}_{4z})$, where $g_o = \epsilon_{zz}k_o^2(\tau_{xy}\tau_{yx} - \tau_{xx}\tau_{yy})$, is a fourth-order polynomial in k_z .¹⁰ Next, define the spectral Green's dyad operators $\tilde{\mathbf{G}}_{ee}(\mathbf{k}; \mathbf{r}') = e^{-i\mathbf{k}\cdot\mathbf{r}'}\text{inv}(\tilde{\mathbf{A}})$ and $\tilde{\mathbf{G}}_{em}(\mathbf{k}; \mathbf{r}') = e^{-i\mathbf{k}\cdot\mathbf{r}'}\text{inv}(\tilde{\mathbf{A}}) \cdot \tilde{\mathbf{V}} \times$ that (respectively) map electric and magnetic sources to the spectral electric field as follows: $\tilde{\mathbf{E}}(\mathbf{k}) = ik_o\eta_o\tilde{\mathbf{G}}_{ee} \cdot \tilde{\mathbf{J}}$ and $\tilde{\mathbf{E}}(\mathbf{k}) = -\tilde{\mathbf{G}}_{em} \cdot \tilde{\mu}_r^{-1} \cdot \tilde{\mathbf{M}}$.

In a homogeneous medium, the integral along k_z in Eq. (2.10) can be performed analytically using the residue theorem. The vector-valued residues are the four supported eigenmode electric fields having propagation constants corresponding to the four roots of $\det(\tilde{\mathbf{A}})$, in terms of which we have the following generic expression for the space-domain (direct) electric field $\mathcal{E}_d(\mathbf{r})$:¹¹

$$\begin{aligned} \mathcal{E}_d(\mathbf{r}) = & \frac{i}{(2\pi)^2} \iint_{-\infty}^{+\infty} \left[u(z-z') \sum_{n=1}^2 \tilde{a}_n \tilde{\mathbf{e}}_n e^{i\tilde{k}_{nz}(z-z')} \right. \\ & \left. + u(z'-z) \sum_{n=3}^4 \tilde{a}_n \tilde{\mathbf{e}}_n e^{i\tilde{k}_{nz}(z-z')} \right] \\ & \times e^{ik_x(x-x') + ik_y(y-y')} dk_x dk_y, \end{aligned} \quad (2.11)$$

where the $\{\tilde{\mathbf{e}}_n(k_x, k_y)\}$ are eigenmode electric field vectors and the $\{\tilde{a}_n(k_x, k_y)\}$ are (source-dependent) modal amplitudes associated with the four eigenvalues [i.e., poles of $\text{inv}(\tilde{\mathbf{A}})$] $\{\tilde{k}_{nz}\}$. In the multilayer case, with \mathbf{r}' in layer M and \mathbf{r} in layer L , a scattered-field contribution $\mathcal{E}_L^s(\mathbf{r})$ is added to $\mathcal{E}_d(\mathbf{r})$ so that the total electric field in layer L writes as

$\mathcal{E}_L(\mathbf{r}) = \delta_{LM}\mathcal{E}_d(\mathbf{r}) + \mathcal{E}_L^s(\mathbf{r})$, where

$$\begin{aligned} \mathcal{E}_L^s(\mathbf{r}) = & \frac{i}{(2\pi)^2} \iint_{-\infty}^{+\infty} \left[(1 - \delta_{LN}) \sum_{n=1}^2 \tilde{a}_{L,n}^s \tilde{\mathbf{e}}_{L,n} e^{i\tilde{k}_{L,nz}z} \right. \\ & \left. + (1 - \delta_{L1}) \sum_{n=3}^4 \tilde{a}_{L,n}^s \tilde{\mathbf{e}}_{L,n} e^{i\tilde{k}_{L,nz}z} \right] \\ & \times e^{ik_x(x-x') + ik_y(y-y')} dk_x dk_y, \end{aligned} \quad (2.12)$$

an additional subscript is introduced to denote the layer number (e.g., L in this case), δ_{pq} denotes the Kronecker delta, and the $\{\tilde{a}_{L,n}^s(k_x, k_y)\}$ represent the (source-dependent) scattered-field modal amplitudes. The four modal terms inside both the direct and scattered-field integrals above can be classified into two upward and two downward propagation modes, distinguished according to the signs of $\{\text{Im}(\tilde{k}_{L,nz})\}$.¹²

To expedite propagating the source fields to \mathbf{r} , which requires enforcing continuity of the tangential EM field components throughout the environment, instead of working with Eqs. (2.11)–(2.12) directly it is more convenient to work with a 4×1 vector composed of the four tangential EM field components (see Ref. [24]): $\mathcal{V} = [\mathcal{E}_x \ \mathcal{E}_y \ \mathcal{H}_x \ \mathcal{H}_y]$. The two longitudinal field components can be subsequently obtained from the transverse components [24]. Equations analogous to Eqs. (2.11)–(2.12) thus arise, with \mathcal{E}_L replaced by \mathcal{V}_L , which writes as

$$\mathcal{V}_L(\mathbf{r}) = \frac{i}{(2\pi)^2} \iint_{-\infty}^{+\infty} \mathbf{W}_L(k_x, k_y; z) e^{ik_x(x-x') + ik_y(y-y')} dk_x dk_y. \quad (2.13)$$

III. INTEGRAND MANIPULATIONS

For some (k_x, k_y) that defines the transverse phase variation $\exp[ik_x(x-x') + ik_y(y-y')]$ common to all the plane wave modes within the environment, one desires the total modal contribution $\mathbf{W}_L(k_x, k_y; z)\exp[ik_x(x-x') + ik_y(y-y')]$ at \mathbf{r} . Assuming this transverse phase variation $\exp[ik_x(x-x') + ik_y(y-y')]$, Maxwell's equations for a homogeneous medium can be manipulated [24] to yield the state matrix shown in Eq. (3.2). After substituting in a given layer's constitutive properties, its solution yields the four modal state vectors supported in that layer along with the corresponding modal (axial) propagation constants; this process, repeated for all N layers, is the starting point of procuring $\mathbf{W}_L(k_x, k_y; z)$.¹³ Subsequently, knowledge of the transverse modal fields in each layer combined with enforcement of tangential field continuity across layer interfaces allows one to propagate the radiated

⁸Field quantities (besides \mathbf{k}) exhibiting purely spectral dependence have an over-tilde and are denoted spectral quantities. Furthermore, modal (nonmodal) spectral field quantities appear in lower (upper) case.

⁹ $\delta(\mathbf{r}-\mathbf{r}') = \delta(x-x')\delta(y-y')\delta(z-z')$ is the three-dimensional Dirac delta function.

¹⁰ $\tilde{\tau}_r = \tilde{\mu}_r^{-1}$

¹¹ $u(\cdot)$ represents the Heaviside unit-step function.

¹²The eigenvalues $\{\tilde{k}_{L,1z}, \tilde{k}_{L,2z}, \tilde{k}_{L,3z}, \tilde{k}_{L,4z}\}$ correspond to the propagation constants of the (respectively) Type I up-going, Type II up-going, Type I down-going, and Type II down-going plane wave modes of layer L , and so on for the other $N-1$ layers [24].

¹³The form of Eq. (3.2) differs slightly from formula (2.10.10) in Ref. [24]. The $-i$ factor on both sides of Eq. (3.2), which is embedded into $\tilde{\mathbf{H}}$ on the left side and explicitly shown on the right side, facilitates an eigenvalue/eigenvector problem in which the propagation constants $\{k_{m,nz}\}$ are the sought-after values rather than the $\{ik_{m,nz}\}$ values procured in Ref. [24].

fields to \mathbf{r} in layer L . Note that given the transverse EM fields of the n th mode, the complete six-component, z -independent modal field vector $\{\tilde{\mathbf{e}}_n, \tilde{\mathbf{h}}_n\}$ is completely determined [24].

A. Modal eigenvectors and eigenvalues

The characteristic plane wave modes for an arbitrarily anisotropic layer m are summarily described by the four eigenvalues $(\tilde{k}_{m,1z}, \tilde{k}_{m,2z}, \tilde{k}_{m,3z}, \tilde{k}_{m,4z})$ and the four corresponding 4×1 eigenvectors $[\tilde{\mathbf{s}}_{m,1}, \tilde{\mathbf{s}}_{m,2}, \tilde{\mathbf{s}}_{m,3}, \tilde{\mathbf{s}}_{m,4}]$ of the 4×4 state matrix $\tilde{\mathbf{H}} = \tilde{\mathbf{H}}(k_x, k_y)$. Defining the n th eigenvector as

$$\tilde{\mathbf{s}}_{m,n} = \tilde{\mathbf{s}}_{m,n}(k_x, k_y) = \begin{bmatrix} \tilde{e}_{m,nx} \\ \tilde{e}_{m,ny} \\ \tilde{h}_{m,nx} \\ \tilde{h}_{m,ny} \end{bmatrix} \quad (3.1)$$

and noting that the corresponding n th characteristic solution $\mathbf{v}_{m,n}$ to

$$\tilde{\mathbf{H}} \cdot \mathbf{v}_{m,n} = -i \frac{\partial}{\partial z} \mathbf{v}_{m,n} \quad (3.2)$$

has the form $\mathbf{v}_{m,n} = \tilde{\mathbf{s}}_{m,n} e^{i\tilde{k}_{m,nz}(z-z^*)}$, one can show that the eigenmode problem $\tilde{\mathbf{H}} \cdot \tilde{\mathbf{s}}_{m,n} = \tilde{k}_{m,nz} \tilde{\mathbf{s}}_{m,n}$ results.

To facilitate accurate and rapid numerical eigenmode computation, the following relations comprise analytical changes made to the canonical eigenmode formulations for isotropic media [24], reciprocal, electrically uniaxial media [28], and generally anisotropic media (i.e., via the state matrix $\tilde{\mathbf{H}}$) [24]:

$$\begin{aligned} k_x &\rightarrow k_o(k_x/k_o) = k_o k_{xr}, \\ k_y &\rightarrow k_o(k_y/k_o) = k_o k_{yr}, \\ \omega \mu_o &\rightarrow k_o \eta_o, \text{ and } \omega \epsilon_o \rightarrow k_o / \eta_o. \end{aligned} \quad (3.3)$$

Accurate computation of the eigenvectors and eigenvalues is of paramount importance to achieving high-precision results. This is because, as will be seen throughout this section, every mixed-domain field quantity is dependent upon the eigenvectors and/or eigenvalues.

B. Intrinsic reflection and transmission matrices

We next calculate the 2×2 intrinsic reflection and transmission matrices.¹⁴ If down-going incident fields in layer m are phase referenced¹⁵ to $z = z_m$, then $\tilde{\mathbf{R}}_{m,m+1}$ and $\tilde{\mathbf{T}}_{m,m+1}$ are easily procured [24] (see Fig. 2 below for an illustration of the scattering problem for downward incident modal fields); similar holds for $\tilde{\mathbf{R}}_{m+1,m}$ and $\tilde{\mathbf{T}}_{m+1,m}$.

C. Generalized reflection and three-layer transmission matrices

With the intrinsic reflection and transmission matrices now available, we derive the generalized reflection matrices (GRM) and three-layer transmission matrices (3TM). The 3TM yields the total down-going (up-going) fields in the slab layer of the

¹⁴“Intrinsic” refers to reflection and transmission matrix quantities associated with only two media present (see Fig. 2)

¹⁵Fields “phase-referenced” to z^* possess a $\exp[i\tilde{k}_{m,nz}(z - z^*)]$ type of z dependence.

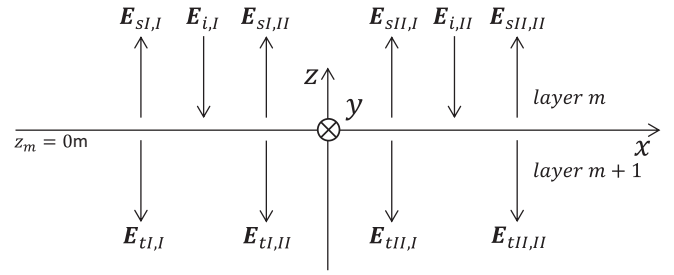


FIG. 2. The incident modes (i,I and i,II subscripts), Type I/II reflected modes due to the incident Type I (sI,I and sI,II subscripts) and Type II modes (sII,I and sII,II subscripts), and Type I/II transmitted modes due to the incident Type I (tI,I and tI,II subscripts) and Type II modes (tII,I and tII,II subscripts) are shown.

canonical three-layer medium problem for incident downward (upward) fields, while the GRM yields the reflected fields in the top (bottom) layer (see Fig. 3).

The GRM assuming down-going incident fields can be determined by looking down into the three bottom-most layers of an N layer medium [respectively labeled as $1'$ (top), $2'$ (middle), and $3'$ (bottom) in Fig. 3] and assuming that the scattered fields in region $2'$ and down-going incident fields in region $1'$ are phase referenced to $z_{2'}$ and $z_{1'}$ (respectively). Following Ref. [24], one imposes two constraint conditions that result in two matrix-valued equations¹⁶

$$\begin{aligned} \tilde{\mathbf{A}}_{2'}^-(z_{1'} - z_{2'}) \cdot \tilde{\mathbf{a}}_{2'}^- \\ = \tilde{\mathbf{T}}_{1'2'} \cdot \tilde{\mathbf{a}}_{1'}^- + \tilde{\mathbf{R}}_{2'1'} \cdot \tilde{\mathbf{A}}_{2'}^+(z_{1'} - z_{2'}) \cdot \tilde{\mathbf{R}}_{2'3'} \cdot \tilde{\mathbf{a}}_{2'}^-, \end{aligned} \quad (3.4)$$

$$\tilde{\mathbf{R}}_{1'2'} \cdot \tilde{\mathbf{a}}_{1'}^- = \tilde{\mathbf{R}}_{1'2'} \cdot \tilde{\mathbf{a}}_{1'}^- + \tilde{\mathbf{T}}_{2'1'} \cdot \tilde{\mathbf{A}}_{2'}^+(z_{1'} - z_{2'}) \cdot \tilde{\mathbf{R}}_{2'3'} \cdot \tilde{\mathbf{a}}_{2'}^-. \quad (3.5)$$

¹⁶The up-going mode eigenvalues are block represented as the 2×2 diagonal matrix $\tilde{\mathbf{A}}_m^+(z) = \exp(\text{diag}[i\tilde{k}_{m,1z}z, i\tilde{k}_{m,2z}z])$, while the down-going mode eigenvalues are block represented as the 2×2 diagonal matrix $\tilde{\mathbf{A}}_m^-(z) = \exp(\text{diag}[i\tilde{k}_{m,3z}z, i\tilde{k}_{m,4z}z])$.

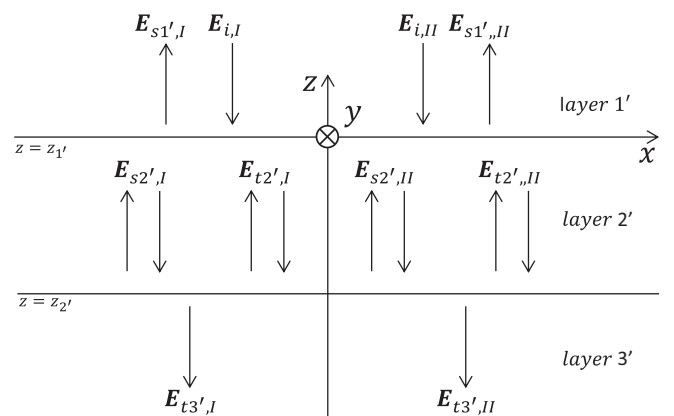


FIG. 3. Schematic depicting the canonical three-layer medium for which the corresponding GRM and 3TM, associated with down-going incident fields in region $1'$, are calculated.

By rearranging Eqs. (3.4) and (3.5), one has¹⁷

$$\tilde{\mathbf{M}} = [\tilde{\mathbf{I}}_2 - \tilde{\mathbf{A}}_{2'}^-(z_{2'} - z_{1'}) \cdot \tilde{\mathbf{R}}_{2'1'} \cdot \tilde{\mathbf{A}}_{2'}^+(z_{1'} - z_{2'}) \cdot \tilde{\mathbf{R}}_{2'3'}] \quad (3.6)$$

and the 3TM

$$\tilde{\mathbf{T}}_{1'2'} = \tilde{\mathbf{M}}^{-1} \cdot \tilde{\mathbf{A}}_{2'}^-(z_{2'} - z_{1'}) \cdot \tilde{\mathbf{T}}_{1'2'} \quad (3.7)$$

with which one has

$$\tilde{\mathbf{a}}_{2'}^- = \tilde{\mathbf{T}}_{1'2'} \cdot \tilde{\mathbf{a}}_{1'}^-. \quad (3.8)$$

Substituting the right-hand side of Eq. (3.8) for $\tilde{\mathbf{a}}_{2'}^-$ in Eq. (3.5), one obtains the GRM

$$\tilde{\mathbf{R}}_{1'2'} = \tilde{\mathbf{R}}_{1'2'} + \tilde{\mathbf{T}}_{2'1'} \cdot \tilde{\mathbf{A}}_{2'}^+(z_{1'} - z_{2'}) \cdot \tilde{\mathbf{R}}_{2'3'} \cdot \tilde{\mathbf{T}}_{1'2'}. \quad (3.9)$$

This procedure can be repeated for layers $N - 3$, $N - 2$, and $N - 1$ by labeling them as layers $1'$, $2'$, and $3'$ (respectively) and replacing $\tilde{\mathbf{R}}_{2'3'}$ in Eq. (3.9) with $\tilde{\mathbf{R}}_{2'3'}$ [24]. The process is recursively performed up to the top three layers. A similar procedure can be used to find the GRM and 3TM looking up into each interface, whose expressions are found by using Eq. (3.8) and Eq. (3.9), labeling the bottom, middle, and top layers as $1'$, $2'$, and $3'$ (respectively), and making the following two variable interchanges in the modified GRM/3TM relations:

$$\tilde{\mathbf{A}}_{2'}^+(z_{1'} - z_{2'}) \leftrightarrow \tilde{\mathbf{A}}_{2'}^-(z_{2'} - z_{1'}), \quad (3.10)$$

$$\tilde{\mathbf{a}}_{m'}^+ \leftrightarrow \tilde{\mathbf{a}}_{m'}^-(m = 1, 2, 3). \quad (3.11)$$

While the procedure above is analytically exact, to avoid the risk of numerical overflow one should shift the reference depth of the slab's transmitted fields to the observation point depth z when the slab contains \mathbf{r} . This avoids propagating downward the up-going modes (or vice versa) at the final stage of assembling the total mixed-domain field $\mathbf{W}_L(k_x, k_y; z)$. Otherwise, exponentially increasing propagators would be present, which may cause numerical overflow. To find the numerically stable 3TM and GRM expressions, we perform similar manipulations as before to obtain:

$$\tilde{\mathbf{M}} = [\tilde{\mathbf{I}}_2 - \tilde{\mathbf{A}}_{2'}^-(z - z_{1'}) \cdot \tilde{\mathbf{R}}_{2'1'} \cdot \tilde{\mathbf{A}}_{2'}^+(z_{1'} - z_{2'}) \cdot \tilde{\mathbf{R}}_{2'3'} \cdot \tilde{\mathbf{A}}_{2'}^-(z_{2'} - z)], \quad (3.12)$$

$$\tilde{\mathbf{a}}_{2'}^- = \tilde{\mathbf{M}}^{-1} \cdot \tilde{\mathbf{A}}_{2'}^-(z - z_{1'}) \cdot \tilde{\mathbf{T}}_{1'2'} \cdot \tilde{\mathbf{a}}_{1'}^- = \tilde{\mathbf{T}}_{1'2'} \cdot \tilde{\mathbf{a}}_{1'}^-, \quad (3.13)$$

$$\tilde{\mathbf{R}}_{1'2'} = \tilde{\mathbf{R}}_{1'2'} + \tilde{\mathbf{T}}_{2'1'} \cdot \tilde{\mathbf{A}}_{2'}^+(z_{1'} - z_{2'}) \cdot \tilde{\mathbf{R}}_{2'3'} \cdot \tilde{\mathbf{A}}_{2'}^-(z_{2'} - z) \cdot \tilde{\mathbf{T}}_{1'2'}. \quad (3.14)$$

D. Direct field modal amplitudes

We next procure the direct field modal amplitudes. For simplicity, the layer-number notation is omitted in this subsection with the understanding that all field quantities are associated with layer M .

If the eigenvalues are unique, we first obtain $\tilde{\mathbf{H}}$ from $\tilde{\mathbf{E}}$ to form the four-component vector $\tilde{\mathbf{V}} = [\tilde{E}_x \ \tilde{E}_y \ \tilde{H}_x \ \tilde{H}_y]$. With

this, we perform the analytic k_z integration of $\tilde{\mathbf{V}} e^{i\mathbf{k}\cdot\mathbf{r}}$ to obtain

$$e^{ik_x(x-x') + ik_y(y-y')} 2\pi i \sum_{l=l_1}^{l_2} [(k_z - \tilde{k}_{lz}) \tilde{\mathbf{V}} e^{ik_z(z-z')}] \Big|_{k_z=\tilde{k}_{lz}}. \quad (3.15)$$

Equivalently, by setting $\tilde{\mathbf{V}}' = \tilde{\mathbf{V}} e^{ik_z(z^* - z')}$, one obtains

$$e^{ik_x(x-x') + ik_y(y-y')} 2\pi i \sum_{l=l_1}^{l_2} [(k_z - \tilde{k}_{lz}) \tilde{\mathbf{V}}' e^{ik_z(z-z^*)}] \Big|_{k_z=\tilde{k}_{lz}}, \quad (3.16)$$

where the sum runs over the two up-going modes [denoted by the substitutions $(l_1, l_2) \rightarrow (1, 2)$ and $z^* \rightarrow z_{M-1}^*$] or two down-going modes [denoted by the substitutions $(l_1, l_2) \rightarrow (3, 4)$ and $z^* \rightarrow z_M^*$], $z_{M-1}^* = \delta_{1M} z' + (1 - \delta_{1M}) z_{M-1}$, and $z_M^* = \delta_{NM} z' + (1 - \delta_{NM}) z_M$. Note that Eq. (3.15) was redefined as Eq. (3.16) to facilitate subsequently calculating reflected and transmitted fields.

Next, defining for up-going mode l ($l = 1, 2$) the tangential fields, obtained after k_z integration followed by suppression of the propagators, as

$$\tilde{\mathbf{u}}_l^* = \tilde{\mathbf{u}}_l^*(k_x, k_y) = [(k_z - \tilde{k}_{lz}) \tilde{\mathbf{V}}] \Big|_{k_z=\tilde{k}_{lz}}, \quad (3.17)$$

$$\tilde{\mathbf{u}}_l = \tilde{\mathbf{u}}_l(k_x, k_y) = [(k_z - \tilde{k}_{lz}) \tilde{\mathbf{V}}'] \Big|_{k_z=\tilde{k}_{lz}}, \quad (3.18)$$

one can define the amplitudes $\tilde{a}_{l,D}^*$ and $\tilde{a}_{l,D}$ (the D subscript stands for direct), corresponding to this mode, which satisfy¹⁸

$$\tilde{\mathbf{u}}_l^* = \tilde{a}_{l,D}^* \tilde{\mathbf{s}}_l, \quad (3.19)$$

$$\tilde{\mathbf{u}}_l = \tilde{a}_{l,D} \tilde{\mathbf{s}}_l. \quad (3.20)$$

If the eigenvalues are degenerate (i.e., when layer M is isotropic), one instead uses the analytically simplified spectral Green's dyads devoid of double poles [29,31,32] when employing Eqs. (3.15)–(3.20). Since the resulting degenerate field is a linear combination of the TE_z and TM_z modes, one follows its evaluation with a TE_z - TM_z modal decomposition. One decomposition example is

$$\begin{bmatrix} \tilde{e}_x^{l+} & \tilde{e}_x^{ll+} \\ \tilde{e}_y^{l+} & \tilde{e}_y^{ll+} \end{bmatrix} \begin{bmatrix} \tilde{a}_D^{l+} \\ \tilde{a}_D^{ll+} \end{bmatrix} = \begin{bmatrix} \tilde{e}_x^+ \\ \tilde{e}_y^+ \end{bmatrix}, \quad (3.21)$$

where \tilde{a}_D^{l+} and \tilde{a}_D^{ll+} are the up-going TE_z and TM_z modal amplitudes (respectively). If using the transverse components leads to an ill-conditioned system, one can use relations in Ref. [24] to find $\tilde{e}_z^{l+}, \tilde{e}_z^{ll+}$ and then solve Eq. (3.21) using \tilde{e}_x and \tilde{e}_z (or \tilde{e}_y and \tilde{e}_z). Note that since Eq. (3.21) is a second-rank linear system, its inversion is trivial; therefore, only the system's conditioning limits the accuracy of the computed amplitudes [33].

E. Scattered mode calculation and field transmission

Now, the total field impinging upon the interfaces $z = z_{M-1}$ and $z = z_M$ must be calculated; this is done via exhibiting and solving the vectorial generalization of relations in Ref. [24] accounting for arbitrary anisotropy (i.e., including intermode

¹⁷The $n \times n$ identity matrix is denoted $\tilde{\mathbf{I}}_n$.

¹⁸Unit-magnitude vectors have an over-hat symbol.

coupling at planar interfaces). All field quantities exhibited below through Eq. (3.27) are associated with layer M .

Define $\tilde{\mathbf{a}}_D^+ = (\tilde{a}_D^{I+}, \tilde{a}_D^{II+})$, $\tilde{\mathbf{a}}_{S1}^+$, and $\tilde{\mathbf{a}}_{S1}^-$ as 2×1 vectors containing (respectively) the amplitudes of the direct up-going, scattered up-going, and scattered down-going modes phase referenced to $z = z_{M-1}$. Similarly, define $\tilde{\mathbf{a}}_D^- = (\tilde{a}_D^{I-}, \tilde{a}_D^{II-})$, $\tilde{\mathbf{a}}_{S2}^+$, and $\tilde{\mathbf{a}}_{S2}^-$ for the *same* modes but phase-referenced to $z = z_M$. With this, one defines the following quantities:¹⁹

$$\begin{aligned} \mathbf{f}_D^+(k_x, k_y; z) &= \tilde{\mathbf{S}}_M^+ \cdot \tilde{\mathbf{A}}_M^+(z - z_{M-1}) \cdot \tilde{\mathbf{a}}_D^+, \\ \mathbf{f}_D^-(k_x, k_y; z) &= \tilde{\mathbf{S}}_M^- \cdot \tilde{\mathbf{A}}_M^-(z - z_M) \cdot \tilde{\mathbf{a}}_D^-, \end{aligned} \quad (3.22)$$

$$\begin{aligned} \mathbf{f}_{S1}^+(k_x, k_y; z) &= \tilde{\mathbf{S}}_M^+ \cdot \tilde{\mathbf{A}}_M^+(z - z_{M-1}) \cdot \tilde{\mathbf{a}}_{S1}^+, \\ \mathbf{f}_{S2}^+(k_x, k_y; z) &= \tilde{\mathbf{S}}_M^+ \cdot \tilde{\mathbf{A}}_M^+(z - z_M) \cdot \tilde{\mathbf{a}}_{S2}^+, \end{aligned} \quad (3.23)$$

$$\begin{aligned} \mathbf{f}_{S1}^-(k_x, k_y; z) &= \tilde{\mathbf{S}}_M^- \cdot \tilde{\mathbf{A}}_M^-(z - z_{M-1}) \cdot \tilde{\mathbf{a}}_{S1}^-, \\ \mathbf{f}_{S2}^-(k_x, k_y; z) &= \tilde{\mathbf{S}}_M^- \cdot \tilde{\mathbf{A}}_M^-(z - z_M) \cdot \tilde{\mathbf{a}}_{S2}^-. \end{aligned} \quad (3.24)$$

Subsequently, in layer M we can represent the tangential fields $\mathbf{W}_M(k_x, k_y; z)$ as

$$\mathbf{W}_M(k_x, k_y; z) = \begin{cases} \mathbf{f}_D^+ + \mathbf{f}_{S1}^+ + \mathbf{f}_{S1}^-, & z > z' \\ \mathbf{f}_D^- + \mathbf{f}_{S2}^+ + \mathbf{f}_{S2}^-, & z < z' \end{cases} \quad (3.25)$$

Armed with relations Eqs. (3.22)–(3.25), one now imposes two constraint conditions [24] that yield the relations (i) $\tilde{\mathbf{a}}_{S1}^- = \tilde{\mathbf{R}}_{M,M-1} \cdot (\tilde{\mathbf{a}}_D^+ + \tilde{\mathbf{a}}_{S1}^+)$ and (ii) $\tilde{\mathbf{a}}_{S2}^+ = \tilde{\mathbf{R}}_{M,M+1} \cdot (\tilde{\mathbf{a}}_D^- + \tilde{\mathbf{a}}_{S2}^-)$. Using these two constraints along with (i) $\tilde{\mathbf{a}}_{S1}^+ = \tilde{\mathbf{A}}_M^+(z_{M-1} - z_M) \cdot \tilde{\mathbf{a}}_{S2}^+$ and (ii) $\tilde{\mathbf{a}}_{S2}^- = \tilde{\mathbf{A}}_M^-(z_M - z_{M-1}) \cdot \tilde{\mathbf{a}}_{S1}^-$, which arise from enforcing continuity of the scattered fields at $z = z'$,

$$\mathbf{W}_L(k_x, k_y; z) = (\tilde{\mathbf{A}}_L^+([z - z_1]\delta_{L1}) \cdot \tilde{\mathbf{S}}_L^+ + (1 - \delta_{L1})\tilde{\mathbf{S}}_L^- \cdot \tilde{\mathbf{A}}_L^-(z - z_{L-1}) \cdot \tilde{\mathbf{R}}_{L,L-1} \cdot \tilde{\mathbf{A}}_L^+(z_{L-1} - z)) \cdot \tilde{\mathbf{a}}_L^+, \quad (3.32)$$

$$\mathbf{W}_L(k_x, k_y; z) = (\tilde{\mathbf{A}}_L^-([z - z_{N-1}]\delta_{LN}) \cdot \tilde{\mathbf{S}}_L^- + (1 - \delta_{LN})\tilde{\mathbf{S}}_L^+ \cdot \tilde{\mathbf{A}}_L^+(z - z_L) \cdot \tilde{\mathbf{R}}_{L,L+1} \cdot \tilde{\mathbf{A}}_L^-(z_L - z)) \cdot \tilde{\mathbf{a}}_L^-. \quad (3.33)$$

If $L = M$, then for $N < M < 1$, one instead obtains $\tilde{\mathbf{a}}_{S1}^-$ and $\tilde{\mathbf{a}}_{S2}^+$ and propagates these to z . Note that this method obviates propagating downward (upward) $\tilde{\mathbf{a}}_{S1}^+$ ($\tilde{\mathbf{a}}_{S2}^-$), thereby preventing another potential source of numerical overflow. The up-going (down-going) direct fields, as phase-referenced to z' , can be propagated to z for $z > z'$ ($z < z'$). Now recall Eq. (3.19) and define $\tilde{\mathbf{a}}_D^{+*} = (\tilde{a}_{1,D}^*, \tilde{a}_{2,D}^*)$ and $\tilde{\mathbf{a}}_D^{-*} = (\tilde{a}_{3,D}^*, \tilde{a}_{4,D}^*)$. Then for $z > z'$ ($z < z'$), $\mathbf{W}_L(k_x, k_y; z)$ writes as (respectively)

$$\begin{aligned} \mathbf{W}_L(k_x, k_y; z) &= \tilde{\mathbf{S}}_L^+ \cdot \tilde{\mathbf{A}}_L^+(z - z') \cdot \tilde{\mathbf{a}}_D^{+*} \\ &+ \tilde{\mathbf{S}}_L^+ \cdot \tilde{\mathbf{A}}_L^+(z - z_L) \cdot \tilde{\mathbf{a}}_{S2}^+ \\ &+ \tilde{\mathbf{S}}_L^- \cdot \tilde{\mathbf{A}}_L^-(z - z_{L-1}) \cdot \tilde{\mathbf{a}}_{S1}^-, \end{aligned} \quad (3.34)$$

upon performing algebraic manipulation one has $\tilde{\mathbf{a}}_{S1}^+$ and $\tilde{\mathbf{a}}_{S2}^-$ as functions of $\tilde{\mathbf{a}}_D^+$ and $\tilde{\mathbf{a}}_D^-$:

$$\begin{aligned} \tilde{\mathbf{M}}_1 &= \tilde{\mathbf{A}}_M^-(z_M - z_{M-1}) \cdot \tilde{\mathbf{R}}_{M,M-1}, \\ \tilde{\mathbf{M}}_2 &= \tilde{\mathbf{A}}_M^+(z_{M-1} - z_M) \cdot \tilde{\mathbf{R}}_{M,M+1}, \end{aligned} \quad (3.26)$$

$$\tilde{\mathbf{a}}_{S1}^+ = [\tilde{\mathbf{I}}_2 - \tilde{\mathbf{M}}_2 \cdot \tilde{\mathbf{M}}_1]^{-1} \cdot \tilde{\mathbf{M}}_2 \cdot [\tilde{\mathbf{a}}_D^- + \tilde{\mathbf{M}}_1 \cdot \tilde{\mathbf{a}}_D^+],$$

$$\tilde{\mathbf{a}}_{S2}^- = [\tilde{\mathbf{I}}_2 - \tilde{\mathbf{M}}_1 \cdot \tilde{\mathbf{M}}_2]^{-1} \cdot \tilde{\mathbf{M}}_1 \cdot [\tilde{\mathbf{a}}_D^+ + \tilde{\mathbf{M}}_2 \cdot \tilde{\mathbf{a}}_D^-]. \quad (3.27)$$

For $L \neq M$, one then uses the sum $\tilde{\mathbf{a}}_D^+ + \tilde{\mathbf{a}}_{S1}^+$ ($\tilde{\mathbf{a}}_D^- + \tilde{\mathbf{a}}_{S2}^-$) and the 3TM matrices to find $\tilde{\mathbf{a}}_L^+$ ($\tilde{\mathbf{a}}_L^-$) for $L < M$ ($L > M$), which write as (respectively)

$$\begin{aligned} \tilde{\mathbf{a}}_L^+ &= \tilde{\mathbf{T}}_{L+1,L} \cdots [\tilde{\mathbf{A}}_{M-2}^+(z_{M-3} - z_{M-2}^{\text{ref}}) \cdot \tilde{\mathbf{T}}_{M-1,M-2}] \\ &\cdot [\tilde{\mathbf{A}}_{M-1}^+(z_{M-2} - z_{M-1}^{\text{ref}}) \cdot \tilde{\mathbf{T}}_{M,M-1}] \cdot (\tilde{\mathbf{a}}_D^+ + \tilde{\mathbf{a}}_{S1}^+), \end{aligned} \quad (3.28)$$

$$\begin{aligned} \tilde{\mathbf{a}}_L^- &= \tilde{\mathbf{T}}_{L-1,L} \cdots [\tilde{\mathbf{A}}_{M+2}^-(z_{M+2} - z_{M+2}^{\text{ref}}) \cdot \tilde{\mathbf{T}}_{M+1,M+2}] \\ &\cdot [\tilde{\mathbf{A}}_{M+1}^-(z_{M+1} - z_{M+1}^{\text{ref}}) \cdot \tilde{\mathbf{T}}_{M,M+1}] \cdot (\tilde{\mathbf{a}}_D^- + \tilde{\mathbf{a}}_{S2}^-), \end{aligned} \quad (3.29)$$

where for some intermediate layer $m \neq L$, z_m^{ref} is the user-defined phase-reference depth.²⁰ Given $\tilde{\mathbf{a}}_L^+$ ($\tilde{\mathbf{a}}_L^-$) for $L < M$ ($L > M$), one then finds $\tilde{\mathbf{a}}_L^-$ ($\tilde{\mathbf{a}}_L^+$) as (respectively)

$$\tilde{\mathbf{a}}_L^- = \tilde{\mathbf{A}}_L^-(z - z_{L-1}) \cdot \tilde{\mathbf{R}}_{L,L-1} \cdot \tilde{\mathbf{A}}_L^+(z_{L-1} - z) \cdot \tilde{\mathbf{a}}_L^+, \quad (3.30)$$

$$\tilde{\mathbf{a}}_L^+ = \tilde{\mathbf{A}}_L^+(z - z_L) \cdot \tilde{\mathbf{R}}_{L,L+1} \cdot \tilde{\mathbf{A}}_L^-(z_L - z) \cdot \tilde{\mathbf{a}}_L^-. \quad (3.31)$$

With the above in mind, we have the following expressions when $L < M$ ($L > M$) (respectively):

$$\begin{aligned} \mathbf{W}_L(k_x, k_y; z) &= \tilde{\mathbf{S}}_L^- \cdot \tilde{\mathbf{A}}_L^-(z - z') \cdot \tilde{\mathbf{a}}_D^{-*} \\ &+ \tilde{\mathbf{S}}_L^+ \cdot \tilde{\mathbf{A}}_L^+(z - z_L) \cdot \tilde{\mathbf{a}}_{S2}^+ \\ &+ \tilde{\mathbf{S}}_L^- \cdot \tilde{\mathbf{A}}_L^-(z - z_{L-1}) \cdot \tilde{\mathbf{a}}_{S1}^-. \end{aligned} \quad (3.35)$$

If $L = M = 1$ or $L = M = N$, one uses $\tilde{\mathbf{a}}_D^-$ or $\tilde{\mathbf{a}}_D^+$ (respectively) to find $\tilde{\mathbf{a}}_{S2}^+ = \tilde{\mathbf{R}}_{1,2} \cdot \tilde{\mathbf{a}}_D^-$ or $\tilde{\mathbf{a}}_{S1}^- = \tilde{\mathbf{R}}_{N,N-1} \cdot \tilde{\mathbf{a}}_D^+$ (respectively). Subsequently, the up-going (down-going) reflected fields are propagated to z . Furthermore, $\tilde{\mathbf{a}}_D^{+*}$ ($\tilde{\mathbf{a}}_D^{-*}$) is propagated to z when $z > z'$ ($z < z'$). With this, for $M = 1$ ($M = N$)

¹⁹The up-going mode eigenvectors are block represented as the 4×2 matrix $\tilde{\mathbf{S}}_m^+ = [\tilde{s}_{m,1} \ \tilde{s}_{m,2}]$, while the down-going mode eigenvectors are block represented as the 4×2 matrix $\tilde{\mathbf{S}}_m^- = [\tilde{s}_{m,3} \ \tilde{s}_{m,4}]$.

²⁰If layer L corresponds to a slab, we compute the 3TM $\tilde{\mathbf{T}}_{L+1,L}$ in (3.28) according to the numerically stable 3TM and GRM formulation presented in Sec. III C. If instead layer L corresponds to the top layer, $\tilde{\mathbf{T}}_{L+1,L}$ reduces to the intrinsic transmission matrix. Similar holds for $\tilde{\mathbf{T}}_{L-1,L}$ in (3.29).

we have (respectively)

$$\begin{aligned} \mathbf{W}_L(k_x, k_y; z) = & u(z - z') \tilde{\mathbf{S}}_L^+ \cdot \tilde{\mathbf{A}}_L^+(z - z') \cdot \tilde{\mathbf{a}}_D^{+*} \\ & + u(z' - z) \tilde{\mathbf{S}}_L^- \cdot \tilde{\mathbf{A}}_L^-(z - z') \cdot \tilde{\mathbf{a}}_D^{-*} \\ & + \tilde{\mathbf{S}}_L^+ \cdot \tilde{\mathbf{A}}_L^+(z - z_1) \cdot \tilde{\mathbf{a}}_{S2}^+, \end{aligned} \quad (3.36)$$

$$\begin{aligned} \mathbf{W}_L(k_x, k_y; z) = & u(z - z') \tilde{\mathbf{S}}_L^+ \cdot \tilde{\mathbf{A}}_L^+(z - z') \cdot \tilde{\mathbf{a}}_D^{+*} \\ & + u(z' - z) \tilde{\mathbf{S}}_L^- \cdot \tilde{\mathbf{A}}_L^-(z - z') \cdot \tilde{\mathbf{a}}_D^{-*} \\ & + \tilde{\mathbf{S}}_L^- \cdot \tilde{\mathbf{A}}_L^-(z - z_{N-1}) \cdot \tilde{\mathbf{a}}_{S1}^-. \end{aligned} \quad (3.37)$$

Note that in all expressions obtained throughout this section, no exponentially rising terms are present since down-going (up-going) modes are always propagated downward (upward), leading to a stable numerical implementation.

IV. INTEGRATION METHODOLOGY

In the numerical evaluation of Eq. (2.13), one repeats the steps in Sec. III for every sampled (k_x, k_y) point, approximating Eq. (2.13) as the double sum

$$\begin{aligned} \mathbf{V}_L(\mathbf{r}) \simeq & \frac{i}{(2\pi)^2} \sum_{p=-P_1}^{P_2} \sum_{q=-Q_1}^{Q_2} \mathbf{W}_L(k_{xq}, k_{yp}; z) \\ & \times e^{ik_{xq}(x-x') + ik_{yp}(y-y')} w(k_{xq}) w(k_{yp}). \end{aligned} \quad (4.1)$$

In Sec. IV A, we describe an efficient methodology to compute the contribution from the pre-extrapolation region $-\xi_1 < \text{Re}(k_x) < \xi_1$ (see Fig. 4). In Sec. IV B, we detail an adaptive implementation of the MWA [14,20,26] tailored for this problem to compute the contribution from the extrapolation region $|k_x| > |\xi_1|$ [20].

A. Pre-extrapolation region

The presence of critical points (i.e., branch points, branch cuts, and slab- and interface-guided mode poles) near the $\text{Re}(k_x)$ axis in the pre-extrapolation region requires a detoured contour to yield a robust numerical integration [24]. Furthermore, the oscillatory nature of $\mathbf{W}_L(k_x, k_y; z) \exp[ik_x(x - x') + ik_y(y - y')]$ and the potentially close proximity of critical points to the detoured contour warrants adaptively integrating to ensure accurate results [19,20] (see Fig. 4).

First we discuss the integration path's initial subdivision and parametrization. Similar to Ref. [19], we define: a maximum detour height d_x , the two points bounding the detour as $k_x = \pm P_k$, and the two points within which one adaptively integrates as $k_x = \pm \xi_1$. All these points are indicated in Fig. 4. The detour path can be parameterized, using the real-valued variable r , as $k_x = r - i \sin(\pi r/P_k)$ and $dk_x = (\partial k_x / \partial r) dr$, where $\partial k_x / \partial r = 1 - i(\pi/P_k) \cos(\pi r/P_k)$ and $-\xi_1 \leq r \leq \xi_1$ [19].

To compute $\pm P_k$, we adapt the procedure described in Ref. [19] to arbitrarily anisotropic media. For a layer p ($p = 1, 2, \dots, N$), we calculate the three eigenvalues of its relative material tensors $\tilde{\epsilon}_{r,p}$ and $\tilde{\mu}_{r,p}$ ($\{\epsilon_{pi}\}, \{\mu_{pi}\}, i = 1, 2, 3$), find $\sqrt{\epsilon_{pi}\mu_{pj}}$ for $i, j = 1, 2, 3$, and take the p th layer effective refractive index n_p ($p = 1, 2, \dots, N$) to be the $\sqrt{\epsilon_{pi}\mu_{pj}}$ value having the real part with the largest magnitude but with imaginary part below a user-defined threshold T . Subsequently we compute $n^+ = \max(|\text{Re}\{n_p\}|)$, which yields a worst-case

scenario for the maximum magnitude of the real part of any poles or branch points near the $\text{Re}(k_x)$ axis. Finally, we set $P_k = l_o k_o (n^+ + 1)$, where $l_o \geq 1$ is a user-defined pre-extrapolation region magnification constant.

Furthermore, defining $\Delta x = |x - x'|$, $\Delta y = |y - y'|$, and $\Delta z = |z - z'|$, we compute the following integration path parameters [19]:

$$d_x = \begin{cases} \frac{1}{\Delta x}, & \Delta x > 1 \\ 1, & \text{otherwise} \end{cases}, \quad (4.2)$$

$$\Delta \xi_x = \begin{cases} \frac{\pi}{\Delta x}, & \Delta x > 1 \\ \pi, & \text{otherwise} \end{cases}, \quad (4.3)$$

$$\xi_1 = \left(\text{Int} \left(\frac{P_k}{\Delta \xi_x} \right) + 1 \right) \Delta \xi_x, \quad (4.4)$$

where $\text{Int}(\cdot)$ truncates its argument to an integer number. Next, we splice the regions $(0, P_k)$ and $(-P_k, 0)$ each into P regions. Letting T_1 and T_2 be two user-defined constants, one has

$$\Delta k = \begin{cases} \frac{\pi}{T_1 \max(\Delta x, \Delta z)}, & \Delta x + \Delta z > 0 \\ \frac{\pi}{T_1 \Delta y}, & \text{otherwise} \end{cases}, \quad (4.5)$$

$$N_{\text{node}} = \text{Int} \left(\frac{P_k}{\Delta k} \right) + 1, \quad (4.6)$$

resulting in $P = \text{Int}(1 + N_{\text{node}}/T_2)$. This empirical methodology for parameterizing and splicing the pre-extrapolation region relies upon the conservative assumption of equidistant sampling.

We utilize a nested Patterson-Gauss quadrature scheme [19] throughout the pre-extrapolation region. Such schemes sacrifice algebraic degrees of precision, yielding only $3n + 1$

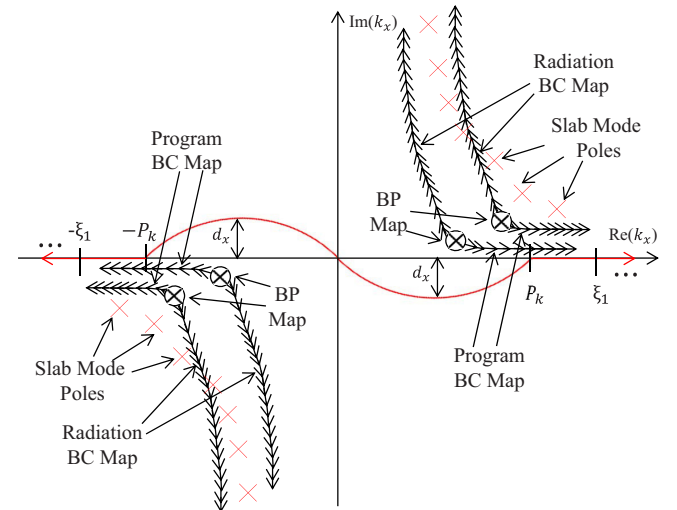


FIG. 4. (Color online) Typical k_x plane features present when evaluating Eq. (2.13). “Radiation BC Map” and “Program BC Map” refer to the branch cuts associated with the radiation condition at infinity and the computer program’s square root convention (respectively). The encircled “X” symbols represent the branch points and the red “X” symbols represent slab- and interface-guided mode poles. For K extrapolation intervals used, the red contour represents the integration path extending to $k_x = \pm \xi_{K+1}$.

$(3n + 2)$ degrees of precision for n odd (even) when adding on $n + 1$ nested quadrature nodes [34,35], in contrast to $4n + 1$ degrees of precision for a $(2n + 1)$ -point Gauss quadrature formula [36]. However, considering the extensive calculations involved at each sampled (k_x, k_y) node (see Sec. III), a Patterson-Gauss scheme significantly reduces the overall computation time [37].

Finally, one folds the integral results from $(0, \xi_1)$ and $(-\xi_1, 0)$ to yield $I'_{x0} = I'_{x0}(k_y)$.

B. Extrapolation region

Subsequently, one must approximate the integral over the path's tails (ξ_1, ∞) and $(-\infty, -\xi_1)$ along the $\text{Re}(k_x)$ axis. For a robust computation, so that both approximation error and convergence rate are good for different geometries and ranges of layer constitutive properties, an integral extrapolation (i.e., acceleration) technique is required. Here we adopt the MWA [14,20,26]²¹ and briefly summarize below the extensions and adaptations made to our problem.²²

(i) Splice the path $(\xi_1, \xi_1 + N\Delta\xi_x)$ into N subintervals²³ with bounding breakpoints $\xi_{xn} = \xi_1 + (n - 1)\Delta\xi_x$ [19,20,26].

(ii) Integrate each subinterval using (for example) a 15- or 20-point Legendre-Gauss quadrature rule [19,26].

(iii) Store these results as I'_{xp} ($p = 1, 2, \dots, N$).

(iv) Repeat steps 1-3 for the path $(-\xi_1 - N\Delta\xi_x, -\xi_1)$ to procure I'_{xp} .

(v) Fold I'_{xp} and I'_{xp} together to form $I'_{xp} = I'_{xp} + I'_{xp}$ ($p = 1, 2, \dots, N$).

(vi) Obtain cumulative integrals $I'_{xp,c}$ via update: $I'_{xp,c} = I'_{xp} + I'_{x(p-1),c}$ ($p = 2, 3, \dots, N$) (Note: $I'_{x1,c} = I'_{x1}$).

(vii) Use the $\{I'_{xp,c}\}$ to estimate the nontruncated tail integral I'_x as $I'_{x(N)}$.

(viii) Compute the complete k_x integral $I'_x = I'_x(k_y) = I'_{x(N)} + I'_{x0}$.

The MWA accelerates convergence of integrals like Eq. (2.13) via estimating the tail integral's truncation error followed by combining two or more estimates, exemplified by

$$I'_{x(N)} = \frac{\sum_{n=1}^{n=N} w_n I'_{xn,c}}{\sum_{n=1}^{n=N} w_n} \quad (4.7)$$

to accelerate the truncation error's decay. First, denote the true truncation error of $I'_{xn,c}$ as R_{xn} such that $I'_{xn,c} = I'_{xn,c} + R_{xn}$. Then, defining $\gamma_{1,2} = w_2/w_1$ and setting $N = 2$, one can rewrite Eq. (4.7) as [20,26]:

$$\begin{aligned} I'_{x(2)} &= \frac{w_1 [I'_x - R_{x1}] + w_2 [I'_x - R_{x2}]}{w_1 + w_2} \\ &= I'_x - R_{x2} \frac{\frac{R_{x1}}{R_{x2}} + \gamma_{1,2}}{1 + \gamma_{1,2}}. \end{aligned} \quad (4.8)$$

²¹More specifically, we employ the the Mosig-Michalski algorithm variant of MWA [38] (MMA for short).

²²It is assumed that (1) one has detoured sufficiently far past any branch points or poles near to the $\text{Re}(k_x)$ axis [19,20,26] and (2) as $|k_x| \rightarrow \infty$, $i\tilde{k}_z(z - z') \rightarrow -f(k_x)\Delta z$, where $f(k_x) = f(-k_x)$ and $\text{Re}(f(k_x)) > 0$.

²³This N is unrelated to the number of layers.

Next, setting $\gamma_{1,2} = -R_{x1}/R_{x2}$ yields $I'_{x(2)} = I'_x$ despite using only two finite-length tail integrals. However, in reality one must estimate the $\{R_{xn}\}$ (thus yielding estimated error ratios $\{-\gamma_{n,n+1}^{\text{est}(1)}\}$) via approximation of the truncation error integral's asymptotic behavior [20]. By folding the asymptotic form of the k_x integral's tail section one has

$$\begin{aligned} &\int_{\xi_1}^{\infty} k_x^q e^{-f(k_x)\Delta z} e^{ik_x(x-x')} dk_x + \int_{-\infty}^{-\xi_1} k_x^q e^{-f(k_x)\Delta z} e^{ik_x(x-x')} dk_x \\ &= \int_{\xi_1}^{\infty} 2k_x^q \left\{ \begin{array}{l} \cos k_x(x-x') \\ i \sin k_x(x-x') \end{array} \right\} e^{-f(k_x)\Delta z} dk_x \end{aligned} \quad (4.9)$$

with the sine (cosine) factor for q odd (even). Furthermore, the factor $e^{-f(k_x)\Delta z} k_x^q$ above can be rewritten as $(e^{-f(k_x)\Delta z} k_x^{q+1})/k_x$ to conservatively ensure that in the multilayer case, one can satisfy the assumption [20] that the integrand has the form $h(k_x; z, z') = g(k_x; z, z')p(k_x)$, where $p(k_x)$ is an oscillatory function with period $2T = 2\pi/\Delta x$ and (asymptotically) $g(k_x)$ has the form

$$g(k_x; z, z') \sim \frac{e^{-f(k_x)\Delta z}}{k_x^\alpha} [C + \mathcal{O}(k_x^{-1})] \sim \frac{e^{-f(k_x)\Delta z}}{k_x^\alpha} \sum_{l=0}^{\infty} \frac{c_l}{k_x^l}. \quad (4.10)$$

Adapted to our problem, the analytic remainder estimate takes the form (for $\Delta x > 0$) $R_{xn}^{\text{est}(1)} = (-1)^n e^{-f(k_x)\Delta z} \xi_{n+1}^{q+1}$, where R_{xn} has the asymptotic form $R_{xn,a} \sim R_{xn}^{\text{est}(1)} \sum_{l=0}^{\infty} a_l \xi_{n+1}^{-l}$ [20]. Subsequently, assuming that $R_{xn}/R_{x(n+1)}$ has the asymptotic form $R_{xn}/R_{x(n+1)} = R'_{xn,a} \sim (R_{xn}^{\text{est}(1)}/R_{x(n+1)}^{\text{est}(1)})[1 + \mathcal{O}(\xi_{n+1}^{-2})]$ one can insert $R'_{x1,a}$ and $\gamma_{1,2}^{\text{est}(1)} = -R_{x1}^{\text{est}(1)}/R_{x2}^{\text{est}(1)}$ (in place of $\gamma_{1,2}$) into Eq. (4.8) to obtain [20]

$$\begin{aligned} I'_{x(2)} &= I'_x + R_{x2} \frac{[1 + \mathcal{O}(\xi_2^{-2})] - 1}{1 + 1/\gamma_{1,2}^{\text{est}(1)}} \\ &= I'_x + R_{x2} \frac{\mathcal{O}(\xi_2^{-2})}{1 + 1/\gamma_{1,2}^{\text{est}(1)}} = I'_x - R_{x1}^{(2)} \end{aligned} \quad (4.11)$$

with remainder $R_{x1}^{(2)} = -R_{x2} \mathcal{O}(\xi_2^{-2})/(1 + 1/\gamma_{1,2}^{\text{est}(1)})$. It is seen that $R_{x1}^{(2)}$ is asymptotically equal to R_{x2} except for being scaled by the factor ξ_2^{-2} ; similarly, its corresponding remainder estimate $R_{x1}^{\text{est}(2)}$ is also scaled by ξ_2^{-2} [20,26]. The above procedure can be applied recursively to estimate I'_x using N cumulative integrals [20,26]. By defining

$$\gamma_{n,n+1}^{\text{est}(r-1)} = \gamma_{n,n+1}^{\text{est}(1)} (\xi_{n+2}/\xi_{n+1})^{2(r-2)} \quad (r = 3, 4, \dots, N + 1), \quad (4.12)$$

$$I'_{xn,c} = I'_{xn,c} \quad (n = 1, 2, \dots, N), \quad (4.13)$$

$$I'_{x1}^{(N)} = I'_{x(N)}, \quad (4.14)$$

the following expression is obtained in place of Eq. (4.11) [20,26]:

$$\begin{aligned} I'_{xn,c} &= \frac{I'_{xn,c}^{(r-1)} + I'_{x(n+1),c}^{(r-1)} \gamma_{n,n+1}^{\text{est}(r-1)}}{1 + \gamma_{n,n+1}^{\text{est}(r-1)}}, \quad 2 \leq r \leq N, \\ &1 \leq n \leq N - r + 1. \end{aligned} \quad (4.15)$$

Note from Eq. (4.3) that as $|x - x'|$ increases, $\Delta\xi_x$ is reduced. This is done to keep the interval breakpoints at the extrema (nulls) of the cosine (sine) function in Eq. (4.9) [20], as well as sample the integrand at an adequate rate. However, simultaneously shrinking the region (ξ_1, ξ_{N+1}) may cause an undesirable degradation in accuracy. This can be solved via adaptive integration of the tail integral, using additional extrapolation intervals combined with successively higher-order weighted average schemes until convergence ensues.

For implementing an adaptive version of the MMA, one could in principle utilize an N -tier recursive function call chain to evaluate Eq. (4.15). However, this is not efficient since the number of active, simultaneous calls to the function carrying out extrapolation would peak at $N(N + 1)/2$. Instead, precomputing the weights for each desired N -tier scheme prior to integration such that one can simply compute $I'_x{}^{(N)} = I'_{x1}{}^{(N)}$ as

$$I'_{x1}{}^{(N)} = \sum_{n=1}^{n=N} w_{n,N} I'_{xn,c}, \quad (4.16)$$

where $w_{n,N}$ is the n th weight²⁴ ($n = 1, 2, \dots, N$) of the tier- N MMA scheme, is preferred. The three advantages of this strategy are that it (i) obviates extensive recursive function calls, (ii) eliminates the redundancy of recomputing tier N weights for each new k_y node (this is markedly important for 2D integration), and (iii) requires only one weighted average [i.e., Eq. (4.16)], thereby drastically reducing the arithmetic operations associated with each of the $\{I'_{xn,c}\}$ to one multiplication and one final summation versus $\mathcal{O}(2^{N-1})$ total multiplications and additions required to compute $I'_{x1}{}^{(N)}$ via the recursive function call chain approach. Assuming $N_{\max} > 1$ tiers are sought, the precomputation of the weights proceeds as follows ($N = 2, 3, \dots, N_{\max}$):

(i) In computing $w_{n,N}$ ($1 < n \leq N$), admit n intermediate values $\{w_{n,N}^{(1)}, w_{n,N}^{(2)}, \dots, w_{n,N}^{(n)}\}$, where $w_{n,N}^{(1)} = 1$.

(ii) Recall Eq. (4.15) and set $r = 2$. Comparing this with Eq. (4.16), we find $w_{1,2} = 1/(1 + \gamma_{1,2}^{\text{est}(1)})$ and $w_{2,2} = 1/(1 + 1/\gamma_{1,2}^{\text{est}(1)})$. We also set $w_{2,2}^{(1)} = 1$ and $w_{2,2}^{(2)} = w_{2,2}$.

(iii) Recursively compute the $\{w_{1,n}\}$ as $w_{1,m} = \frac{w_{1,m-1}}{1 + \gamma_{1,2}^{\text{est}(m-1)}}$ ($m = 3, 4, \dots, N_{\max}$).

(iv) To compute $w_{n,N}$ ($2 \leq n \leq N$, $N > 2$), first note the $\{w_{n,N}^{(m)}\}$ initially update as

$$w_{n,N}^{(m)} = \frac{w_{n,N-1}^{(m)}}{1 + \gamma_{n-m+1,n-m+2}^{\text{est}(N+m-n-1)}} \quad (m = 1, 2, \dots, n; n \neq N), \quad (4.17)$$

$$w_{n,N}^{(1)} = 1, w_{n,N}^{(2)} = w_{n,N}^{(3)} = \dots = w_{n,N}^{(N)} = 0 \quad (n = N). \quad (4.18)$$

(v) Update the $\{w_{n,N}^{(m)}\}$ again as

$$w_{n,N}^{(m)} = w_{n,N}^{(m)} + \frac{w_{n,N}^{(m-1)}}{1 + 1/\gamma_{n-m+1,n-m+2}^{\text{est}(N+m-n-1)}} \quad (m = 2, 3, \dots, n) \quad (4.19)$$

set $w_{n,N} = w_{n,N}^{(n)}$ to obtain the desired weight, and store the intermediate values for recursive reapplication of steps (iv)–(v).

To clarify steps (iv)–(v), let us take a simple example and outline the process of obtaining the third cumulative integral's weights corresponding to the three-tier, four-tier, and five-tier MMA (i.e., $w_{3,3}$, $w_{3,4}$, and $w_{3,5}$). Starting with $N = 3$ and noting that $n = N = 3$, we apply Eq. (4.18) to obtain $w_{3,3}^{(1)} = 1$ and $w_{3,3}^{(2)} = w_{3,3}^{(3)} = 0$. Second, we apply Eq. (4.19) to obtain $w_{3,3}^{(2)} = 0 + w_{3,3}^{(1)}/(1 + 1/\gamma_{2,3}^{\text{est}(1)})$ and use this updated $w_{3,3}^{(2)}$ value to compute $w_{3,3} = w_{3,3}^{(3)} = 0 + w_{3,3}^{(2)}/(1 + 1/\gamma_{1,2}^{\text{est}(2)})$, yielding one of our desired weights. Third, we use these three updated intermediate values as the input to another application of step (iv) with $N = 4$, using Eq. (4.17) to obtain $w_{3,4}^{(1)} = w_{3,3}^{(1)}/(1 + \gamma_{3,4}^{\text{est}(1)})$, $w_{3,4}^{(2)} = w_{3,3}^{(2)}/(1 + \gamma_{2,3}^{\text{est}(2)})$, and $w_{3,4}^{(3)} = w_{3,3}^{(3)}/(1 + \gamma_{1,2}^{\text{est}(3)})$. Finally, use Eq. (4.19) to obtain $w_{3,4}^{(2)} = w_{3,4}^{(2)} + w_{3,4}^{(1)}/(1 + 1/\gamma_{2,3}^{\text{est}(2)})$ and $w_{3,4} = w_{3,4}^{(3)} = w_{3,4}^{(2)} + w_{3,4}^{(2)}/(1 + 1/\gamma_{1,2}^{\text{est}(3)})$, giving the second desired weight.

The above procedure lends two practical improvements to the original MMA by (i) significantly reducing the operation count involving the $\{I'_{xn,c}\}$ and (ii) devising a numerically stable scheme to efficiently update the weights. After the tail integral has converged, one computes $I'_x = I'_{x1}{}^{(N)} + I'_{x0}$ to yield the final result.

V. RESULTS

We now present a series of numerical results using the formulation presented above for the analysis of well-logging induction (resistivity) tools for geophysical prospecting (compared against Refs. [1–3]) and the field pattern generated by electric current sources supported on grounded dielectric substrates (compared against Ref. [39]). The layers are numbered starting with the layer at the highest elevation and z_B contains the interface depth values.

Induction tools are generally composed of a system of transmitter and receiver loop antennas that can be modeled as Hertzian magnetic dipoles. The parameter L_m denotes the separation between the transmitter and m th receiver (if all receivers are collocated, then $L = L_1$).

The environmental parameter of interest is the resistivity of the surrounding Earth media, which can exhibit electrical anisotropy and planar-stratified inhomogeneity. Earth layers exhibiting reciprocal, electrical uniaxial anisotropy possess different resistivities on and transverse to their respective bedding planes, which are equal to $R_{hn} = 1/\sigma_{hn}$ and $R_{vn} = 1/\sigma_{vn}$ in layer n (respectively). Furthermore, each such layer has a bedding plane with arbitrary misalignment with respect to the z axis, which for layer n is characterized by a dip angle and a strike angle that are denoted as α_n and β_n (respectively). α (β) refers to the tool's polar (azimuthal) rotation relative to the z axis; see Ref. [2] for the formation dip and strike angle convention, which is the same as the tool dip and strike angle convention.

²⁴For a given N , these weights are related to the weights shown in Eq. (4.7) via the relation $w_{n,N} = w_n / \sum_{n=1}^{n=N} w_n$, where the $\{w_n\}$ here tacitly exhibit dependence on N .

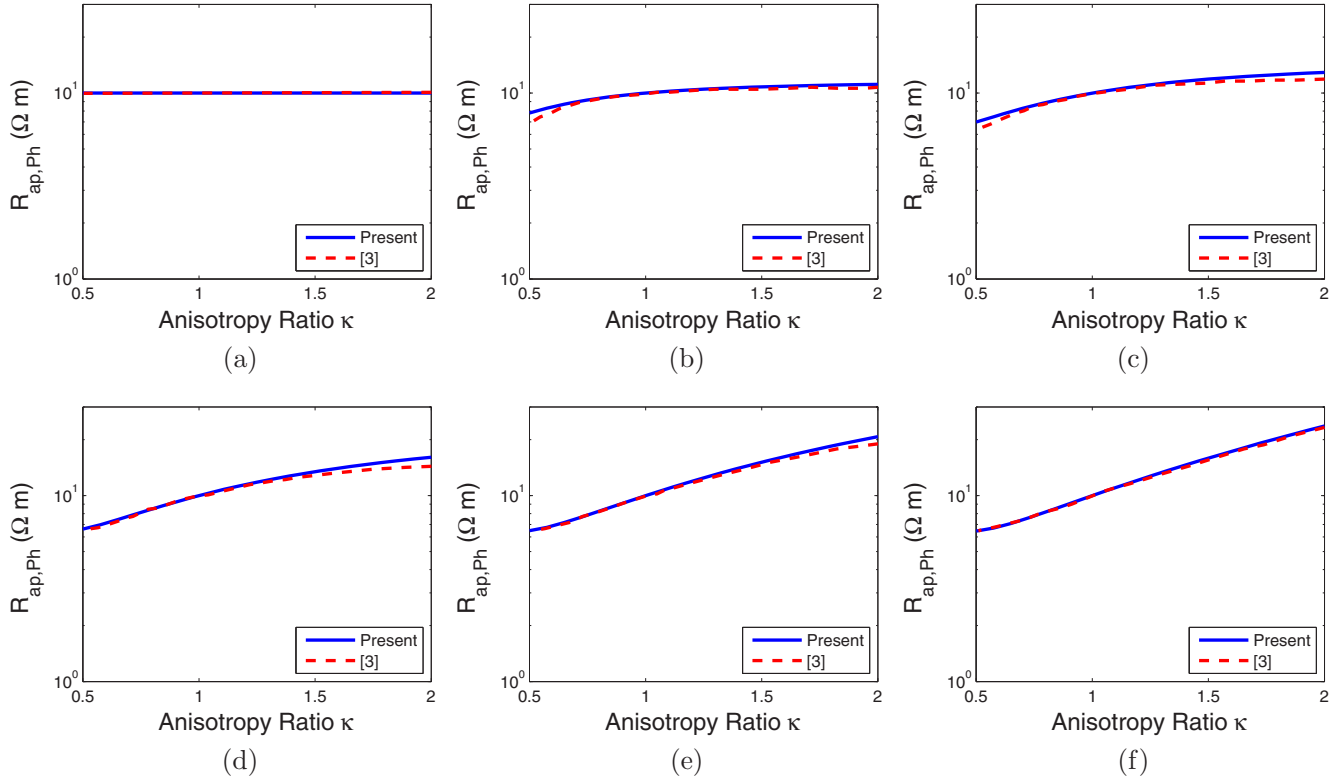


FIG. 5. (Color online) Phase-apparent resistivity log comparison with Fig. 2 of Ref. [3] (homogeneous medium): $R_h = 10 \Omega \text{ m}$, $\beta = 0^\circ$, $f = 2 \text{ MHz}$, $L_1 = 25 \text{ in}$, $L_2 = 31 \text{ in}$. In Figs. 5(a)–5(f) the respective tool dip angles are as follows: $0^\circ, 30^\circ, 45^\circ, 60^\circ, 75^\circ, 90^\circ$.

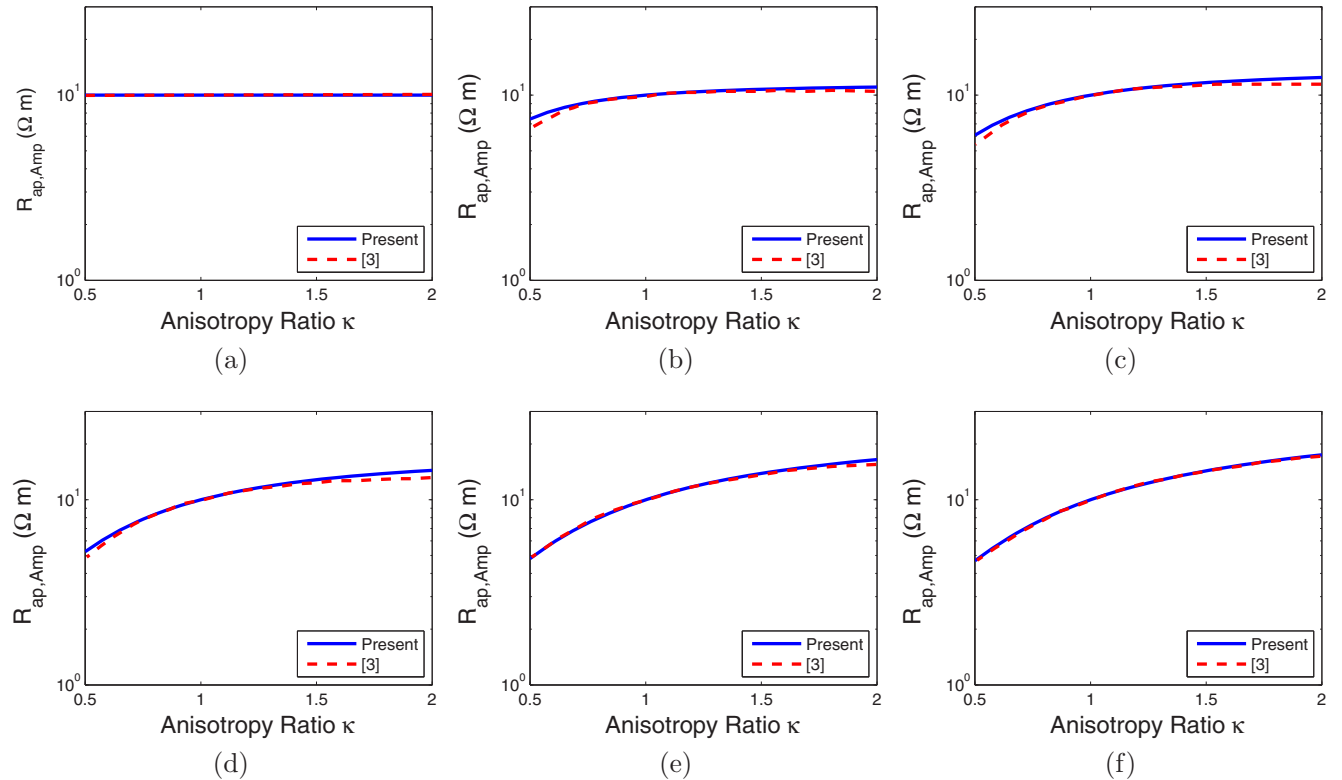


FIG. 6. (Color online) Magnitude-apparent resistivity log comparison with Fig. 3 of Ref. [3] (homogeneous medium): $R_h = 10 \Omega \text{ m}$, $\beta = 0^\circ$, $f = 2 \text{ MHz}$, $L_1 = 25 \text{ in}$, $L_2 = 31 \text{ in}$. In Figs. 6(a)–6(f) the respective tool dip angles are as follows: $0^\circ, 30^\circ, 45^\circ, 60^\circ, 75^\circ, 90^\circ$.

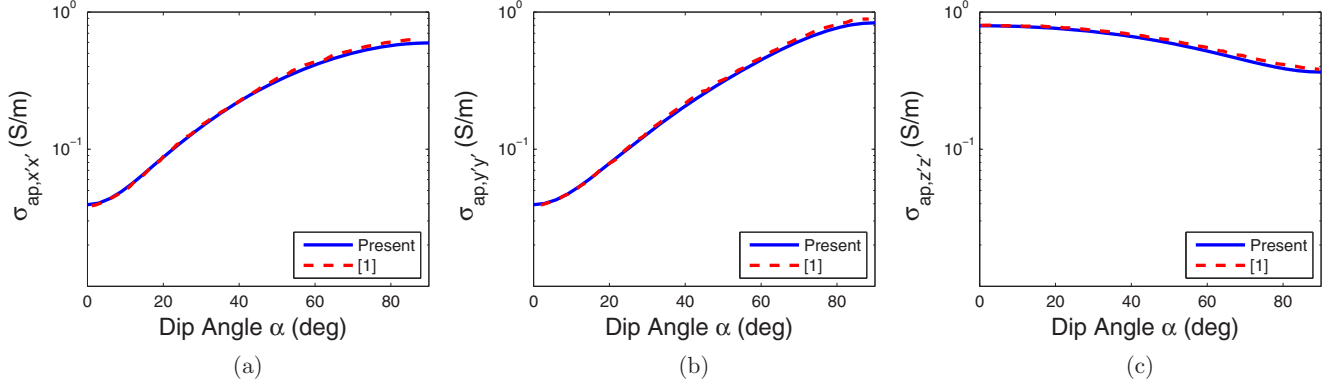


FIG. 7. (Color online) Apparent conductivity log comparison with Fig. 2 of Ref. [1] (homogeneous medium). $\kappa = \sqrt{5}$, $R_h = 1 \Omega \text{ m}$, $\beta = 0^\circ$, $f = 25 \text{ kHz}$, $L = 1 \text{ m}$.

Note that for homogeneous formations characterized by this type of anisotropy, we use the variable α to refer to the tool inclination angle relative to the z -directed optic axis or the tilting of the optic axis relative to the z axis (with a z -directed tool) interchangeably; these definitions are equivalent in homogeneous formations exhibiting isotropy or reciprocal, electrical uniaxial anisotropy [6].

When displacement currents are non-negligible compared to induction currents, the anisotropy ratio of layer n , κ_n , is defined as

$$\kappa_n = \sqrt{(k_o \epsilon_{hn,r} + i \eta_o \sigma_{hn}) / (k_o \epsilon_{vn,r} + i \eta_o \sigma_{vn})}, \quad (5.1)$$

where $\epsilon_{hn,r}$ ($\epsilon_{vn,r}$) is the complex-valued dielectric constant parallel (orthogonal) to the layer's bedding plane [3]. This reduces to $\kappa_n = \sqrt{R_{vn}/R_{hn}} = \sqrt{\sigma_{hn}/\sigma_{vn}}$ [2] when displacement currents are negligible compared to induction currents (i.e., at sufficiently low frequencies). For later reference, we also state the approximate formula predicting the formation resistivity estimated by a standard coaxial induction tool in a homogeneous, uniaxial medium [6]:

$$R_{\text{ap}} = \frac{\kappa R_h}{\sqrt{\sin^2 \alpha + \kappa^2 \cos^2 \alpha}}. \quad (5.2)$$

A. Arrayed coaxial sonde

The first logging scenario simulated here is an arrayed, coaxial induction sonde with one transmitter and two receivers immersed in a homogeneous, uniaxial medium with z -directed optic axis [3]. We vary (i) α and (ii) κ (i.e., fix R_h, ϵ_h and vary R_v, ϵ_v).

To extract effective, homogeneous-medium resistivity information from the observed magnetic field data, we follow the approach explained in Ref. [3], which we summarize here. First define the ratio of the two axial-directed magnetic field²⁵ values, observed at the two receiver loop antennas spaced at distances L_1 and L_2 from the transmitter loop antenna (i.e., H_{z1} and H_{z2} , respectively), as $g_{12} = H_{z1}/H_{z2}$. Also, for some complex-valued phasor quantity F , define its phase as $\angle F$ and its magnitude as $|F|$. Phase-apparent resistivity $R_{\text{ap,Ph}}$ is obtained by first generating a lookup table of $\angle g_{12}$, at a specified

transmitter radiation frequency, as a function of conductivity present in a homogeneous, isotropic medium. Subsequently, when the sonde is immersed in a heterogeneous environment that may contain anisotropic media, one compares the actual observed $\angle g_{12}$ to the lookup table and extracts the effective conductivity. This is finally inverted to obtain phase-apparent resistivity. Similar applies for magnitude-apparent resistivity $R_{\text{ap,Amp}}$, except now working with $|g_{12}|$ rather than $\angle g_{12}$.

We see that throughout Figs. 5–6, agreement is consistently strong. Note that in Figs. 5(a) and 6(a), where $\alpha = 0^\circ$, the sensed resistivity is insensitive to κ . This is because when $\alpha = 0^\circ$ in a homogeneous, uniaxial medium, the coaxial sonde produces only H -mode plane wave spectra with electric field confined to the bedding plane [28]. Furthermore, since the anisotropy ratio κ is swept by keeping R_h and ϵ_h constant while varying R_v and ϵ_v , it is expected that the received signal is independent of κ .

B. Triaxial induction sonde

The next logging scenarios involve a triaxial induction sonde with three mutually orthogonal, co-located transmitters and, spaced apart by a distance L , three mutually orthogonal, co-located receivers (see Ref. [4] and Fig. 1 of Ref. [1]). To invert apparent conductivity from the received magnetic field, formula (18) of Ref. [5] is used.

Figure 7 corresponds to the sonde in a homogeneous, uniaxial medium with varying α ; agreement is excellent. Figure 8 corresponds to a thirteen-layer environment with $\alpha = \beta = 0^\circ$. Note that our depth convention here corresponds to the halfway depth between the transmitters and receivers. Excellent agreement is observed between the results. For the coil separation used, $L = 0.4 \text{ m}$, we notice that the coaxial ($\sigma_{a,z'z'}$) and coplanar ($\sigma_{a,x'x'}$) measurements provide marked resolution of even the thinnest bed present (0.2m thick); see the first spike and first valley from the left edge of Figs. 8(a) and 8(b) (respectively).

C. Coaxial sonde and cross-bedding anisotropy

The next logging scenario simulated corresponds to a 2MHz coaxial sonde vertically traversing inhomogeneous environments. We compare our results against those presented in Ref. [2]. It is important to note that there is an ambiguity in the resistivity inversion method and data postprocessing used in Ref. [2] and hence only a qualitative comparison is made

²⁵That is, the magnetic field component directed along the sonde axis, normal to the area of the coaxial receiver loop antenna.

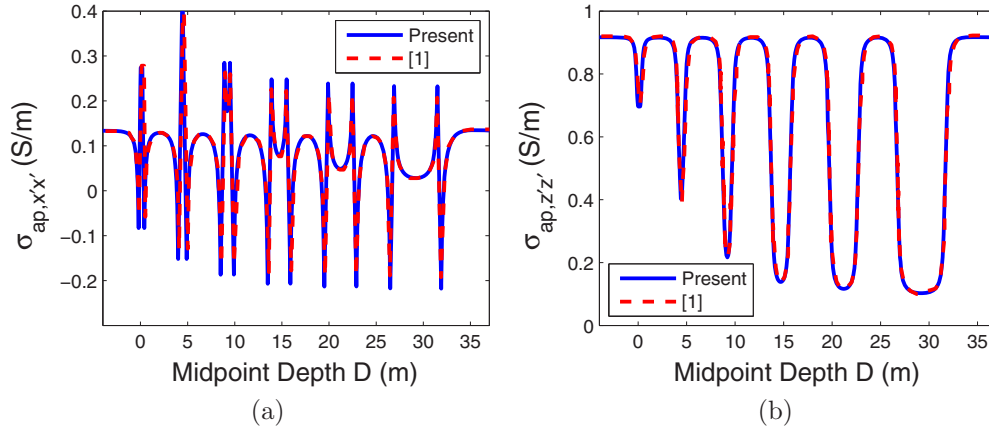


FIG. 8. (Color online) Apparent conductivity log comparison with Fig. 3 of Ref. [1]. $\{\kappa_n\} = \sqrt{5}$ and $\{\alpha_n\} = \{\beta_n\} = 0^\circ$ in all beds; $f = 25$ kHz, $L = 0.4$ m, $\sigma_h = \{1.0, 0.1, 1.0, 0.1, 1.0, 0.1, 1.0, 0.1, 1.0, 0.1, 1.0, 0.1, 1.0\}$ S/m, $z_B = \{0.0, 0.2, 4.2, 4.7, 8.7, 9.7, 13.7, 15.7, 19.7, 22.7, 26.7, 31.7\}$ m.

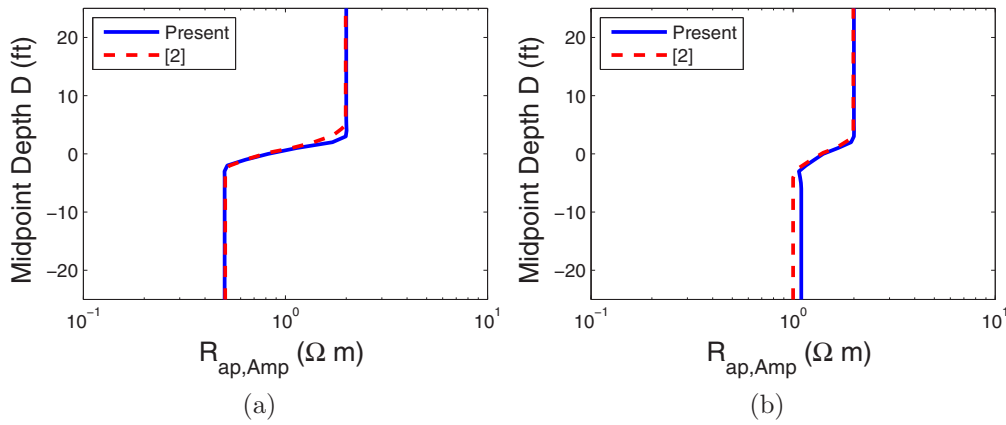


FIG. 9. (Color online) Magnitude-apparent resistivity log comparison with Fig. 6 of Ref. [2]: $\kappa_1 = 1, \kappa_2 = \sqrt{20}, R_{h1} = 2 \Omega$ m, $R_{h2} = 0.5 \Omega$ m, $\beta_2 = 0^\circ$, $f = 2$ MHz, $L = 40$ in, $z_B = 0$ ft. In Figs. 9(a)–9(b) the respective dip angles of the bottom formation are 0° and 60° .

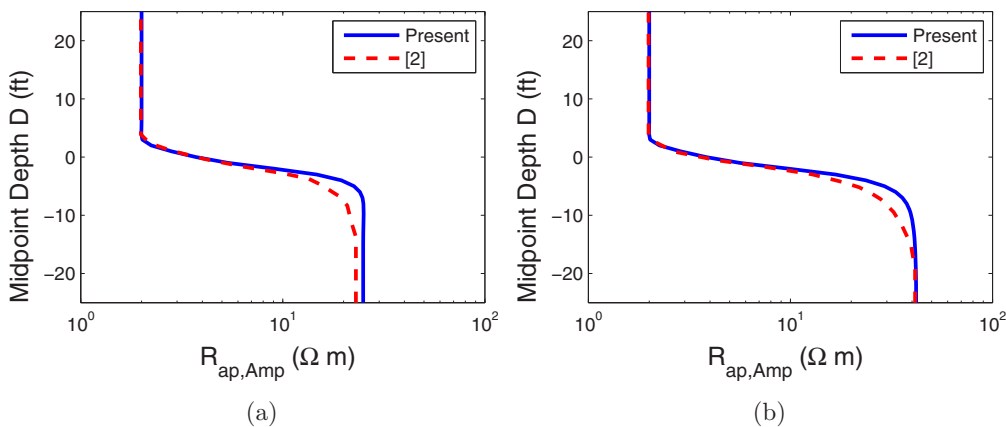


FIG. 10. (Color online) Magnitude-apparent resistivity log comparison with Fig. 7 of Ref. [2]: $\kappa_1 = 1, \kappa_2 = \sqrt{20}, R_{h1} = 2 \Omega$ m, $R_{h2} = 25 \Omega$ m, $\beta_2 = 0^\circ$, $f = 2$ MHz, $L = 40$ in, $z_B = 0$ ft. In Figs. 10(a)–10(b) the respective dip angles of the bottom formation are 0° and 60° .

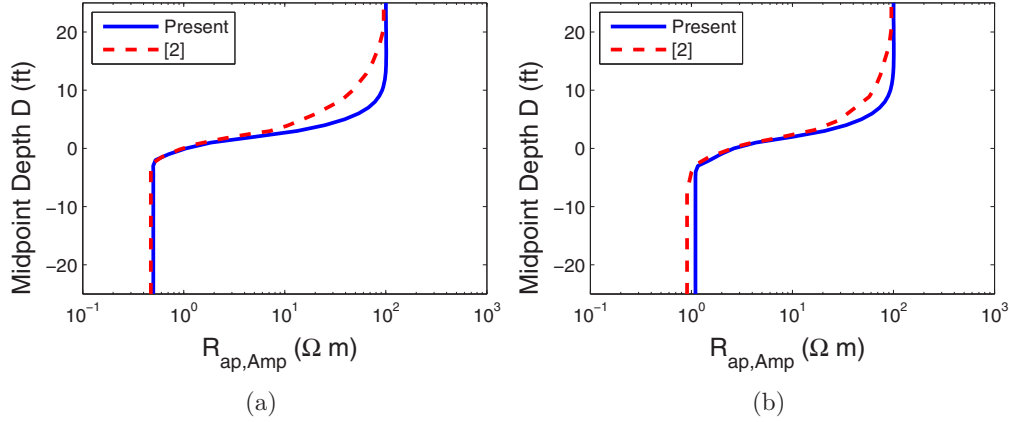


FIG. 11. (Color online) Magnitude-apparent resistivity log comparison with Fig. 8 of Ref. [2]: $\kappa_1 = 1, \kappa_2 = \sqrt{20}, R_{h1} = 100 \Omega \text{ m}, R_{h2} = 0.5 \Omega \text{ m}, \beta_2 = 0^\circ, f = 2 \text{ MHz}, L = 40 \text{ in}, z_B = 0 \text{ ft}$. In Figs. 11(a)–11(b) the respective dip angles of the bottom formation are 0° and 60° .

here. Since the inversion method was not stated explicitly in Ref. [2], we tried different inversion methods and found that the method corresponding to magnitude-apparent effective resistivity, specified in Ref. [3] and summarized above in Sec. V A, produced the best matching results with Ref. [2]. Also, Ref. [2] does not specify the depth convention in their plots (e.g., the transmitter depth). To render our data symmetric with respect to zero depth ($D = 0 \text{ ft}$) in this case, we define the depth D as midway between the receiver and transmitter.

In Fig. 9, where there is a low resistivity contrast of $R_{h1} = 4R_{h2}$, observe that the agreement between the two data sets is good. Note that for Figs. 9(a)–9(b), the effective resistivity in the top isotropic half space levels off to that of the half space’s actual resistivity, as is expected. Furthermore, note in Fig. 9(a) that deep within the bottom uniaxial half space, the effective resistivity levels off to $R_{h2} \sim 0.5 \Omega \text{ m}$, which is consistent with Eq. (5.2). This is because the transmitter antenna produces a primary (i.e., if $\vec{\sigma} = \vec{0}$) $\hat{\phi}'$ -oriented electric field.²⁶ Being oriented perpendicular to the uniaxial medium’s bedding plane, the loop only produces H -mode plane wave

spectra [28] and thus induces azimuthal currents parallel to the bedding plane possessing intensity affected solely by R_{h2} and the top formation’s resistivity. On the other hand, when $\alpha_2 = 60^\circ$, the transmitter loop’s primary electric field now induces currents both parallel and perpendicular to the bedding plane. As a result, now the induced current and sensed resistivity $R_{\text{ap,Amp}}$ is also affected by $R_{v2} = \kappa_2^2 R_{h2}$, leading to a higher value of $R_{\text{ap,Amp}}$ [as qualitatively corroborated by Eq. (5.2)].

In Fig. 10, where there is a high resistivity contrast of $R_{h2} = 12.5R_{h1}$, we notice a greater level of discrepancy. This is particularly so just beneath the interface at $z_B = 0 \text{ ft}$, where the reflected fields are strongest. In the well-logging community, one refers to the phenomenon where conductive formations adversely reduce the apparent resistivity sensed in their resistive neighbors as the shoulder bed effect [40].

In Fig. 11, we again note a high resistivity contrast of $R_{h1} = 200R_{h2}$. Comments dual to those made on Fig. 10 apply here regarding (1) the resistivity log’s notable deviation in the top isotropic region from the true resistivity of $100 \Omega \text{ m}$ and (2) the greater disagreement versus [2].

In Fig. 12, the resistivity contrast is low ($R_{h1} = 4R_{h2}$). Akin to Fig. 9, we note that there is excellent agreement.

²⁶The prime denotes the tool system [4].

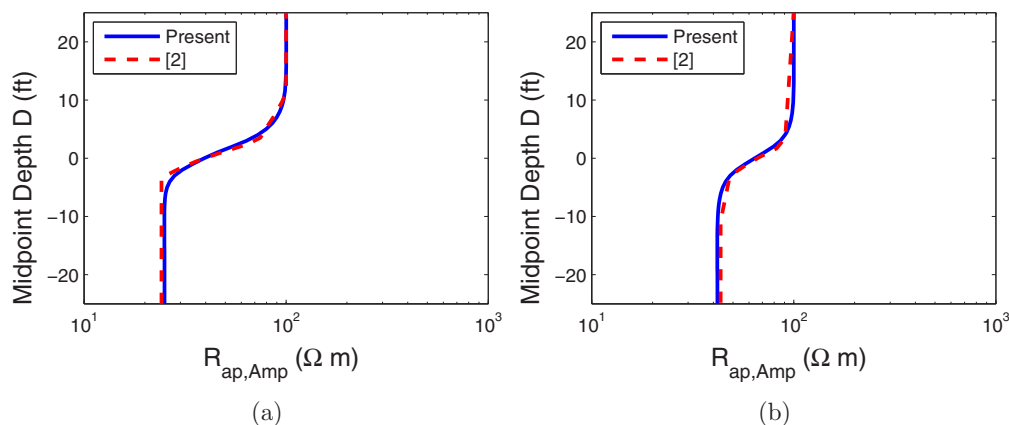


FIG. 12. (Color online) Magnitude-apparent resistivity log comparison with Fig. 9 of Ref. [2]: $\kappa_1 = 1, \kappa_2 = \sqrt{20}, R_{h1} = 100 \Omega \text{ m}, R_{h2} = 25 \Omega \text{ m}, \beta_2 = 0^\circ, f = 2 \text{ MHz}, L = 40 \text{ in}, z_B = 0 \text{ ft}$. In Figs. 12(a)–12(b) the respective dip angles of the bottom formation are 0° and 60° .

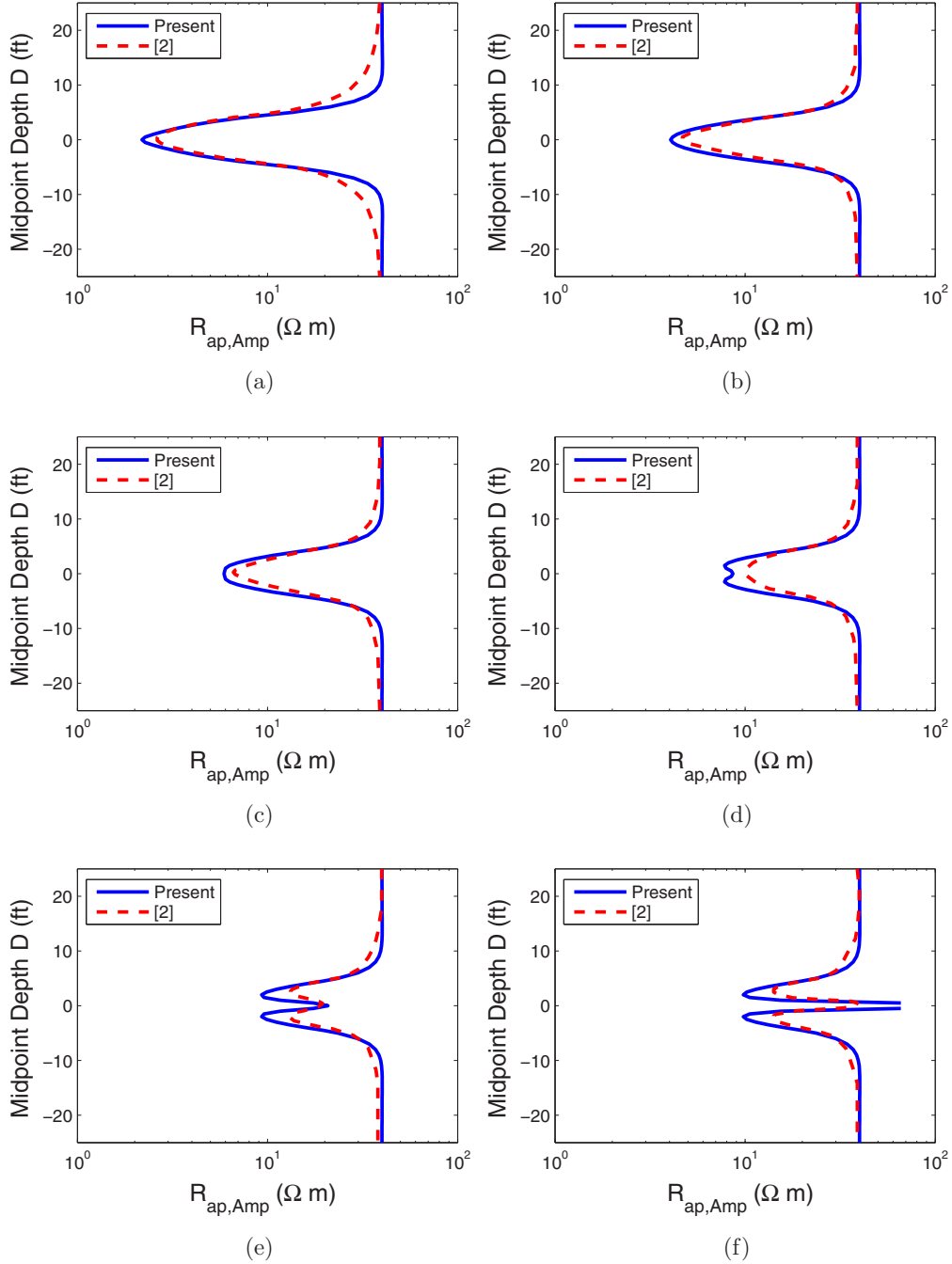


FIG. 13. (Color online) Magnitude-apparent resistivity log comparison with Fig. 11 of Ref. [2]: $\kappa_1 = \kappa_3 = 1, \kappa_2 = 5, R_{h1} = R_{h3} = 40 \Omega \text{ m}, R_{h2} = 2 \Omega \text{ m}, \beta_2 = 0^\circ, f = 2 \text{ MHz}, L = 40 \text{ in}, z_B = \{2.5, -2.5\} \text{ ft}$. In Figs. 13(a)–13(f) the respective dip angles of the center formation are as follows: $0^\circ, 45^\circ, 60^\circ, 70^\circ, 80^\circ, 90^\circ$.

Now we comment upon Figs. 13–14. The data from Ref. [2] suggest a very strong shoulder bed effect present in the top and bottom isotropic half spaces when $\alpha_2 = 0^\circ$, leading to notable disagreement for Figs. 13(a) and 14(a). There is also notable discrepancy in modeling the formation interface horns and resistivity valleys [see, in particular, the infinite-resistivity spike in Fig. 13(f)]. However, the data sets in Ref. [2] are not free of infinite-resistivity spikes either (see Figs. 14 and 23 in Ref. [2]), suggesting that the resistivity inversion and data postprocessing methods used (and their differences between here and Ref. [2]) are causing the observed discrepancies.

These quantitative discrepancies aside, however, we notice excellent qualitative agreement in modeling the shoulder bed effect, as well as the interface horns and valleys due to the high-dipping-angle uniaxial bed.

D. Dipole fields near a PEC-backed microwave substrate

The last validation result concerns a y -directed Hertzian electric dipole on top of a dielectric substrate supported by a metallic ground plane [39]). The ground is modeled as a semi-infinite layer with conductivity $\sigma = 10^9 \text{ S/m}$. We

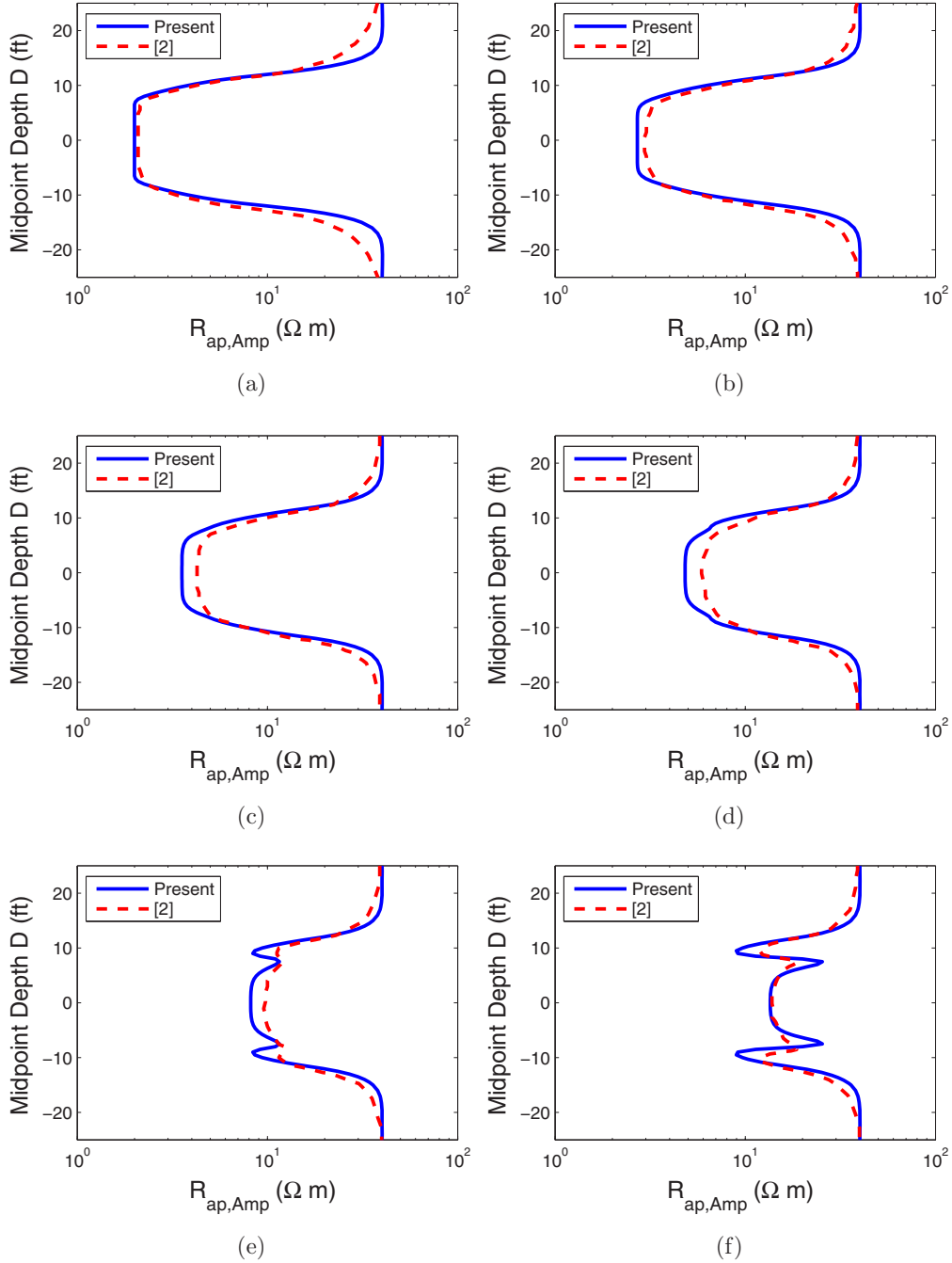


FIG. 14. (Color online) Magnitude-apparent resistivity log comparison with Fig. 13 of Ref. [2]: $\kappa_1 = \kappa_3 = 1, \kappa_2 = 5, R_{h1} = R_{h3} = 40 \Omega \text{ m}, R_{h2} = 2 \Omega \text{ m}, \beta_2 = 0^\circ, f = 2 \text{ MHz}, L = 40 \text{ in}, z_B = \{10, -10\} \text{ ft}$. In Figs. 14(a)–14(f) the respective dip angles of the center formation are as follows: $0^\circ, 45^\circ, 60^\circ, 70^\circ, 80^\circ, 90^\circ$.

compute the radiated H_x , H_z , and E_y components. This environment is meant to highlight the algorithm's ability to simulate magnetic fields produced by an electric, rather than magnetic, source and thus (from the duality theorem) its ability to compute magnetic and electric fields from both electric and magnetic sources. By simulating a case with $4\lambda_o \leq |x - x'| \leq 14\lambda_o$ ($\lambda_o = 37.5 \text{ m}$), we also provide here an example of the general-purpose nature of the algorithm in regards to the $\mathbf{r} - \mathbf{r}'$ geometry. We emphasize that this

flexibility is primarily attributed to the adaptive extension of the original MMA as discussed in Sec. III.

Figure 15(b) below shows excellent agreement, in the range $4.25\lambda_o \leq |x - x'| \leq 13.6\lambda_o$, with the available data from Ref. [39]. Figures 15(a) and 15(c) show similar results for the other two components. The oscillatory behavior results from interference effects caused by the ground plane. To facilitate easier comparison with Ref. [39] and exhibit the three field magnitude variations on identical scales, all three data sets

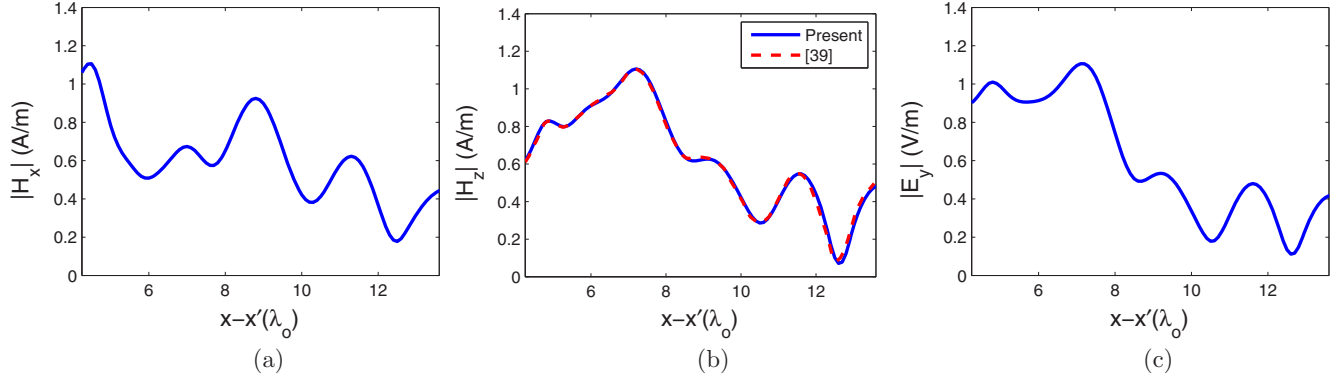


FIG. 15. (Color online) Field component intensities from a y -directed horizontal electric dipole (HED), which is radiating at $f = 8$ MHz ($\lambda_o = 37.5$ m), centered at the origin, and supported on a grounded dielectric substrate $4\lambda_o$ thick with free space above. The substrate's dielectric constant is $\epsilon_r = 3.3(1 + 0.01i)$, while $y - y' = 0$ m and $z - z' = 3$ m. Only $|H_z|$ reference data were published in Ref. [39].

were scaled such that their maximum magnitudes correspond to the maximum magnitude of H_z in Ref. [39].

VI. CONVERGENCE CHARACTERISTICS

To characterize our numerical formulation's ability to converge towards the field solution, we present two case studies concerning the z -directed magnetic field component H_z produced by a z -directed magnetic dipole radiating at $f = 2$ MHz in free space. The first case comprises a benign scenario in which $\mathbf{r} - \mathbf{r}' = (1, 1, 1)$ m, while the second case represents a much more challenging scenario where $\mathbf{r} - \mathbf{r}' = (500, 500, 1)$ m in which the integrand oscillates on the order of 500 times more rapidly than the first case. For both cases, we choose $x - x' = y - y'$ to ensure the code faces the same convergence challenges when evaluating both the k_x and k_y integrals. Furthermore, we set the pre-extrapolation region magnification factor l_o (see Sec. IV A) equal to ten and artificially set $\xi_1 = 2P_k$ to facilitate characterization of the interval subdivision factor h , with which one quantifies the subinterval lengths after full interval subdivision, as $h\xi_1$.

For each case, we present results related to both the pre-extrapolation and extrapolation domain characteristics. To avoid mixing the numerical formulation's handling of the pre-extrapolation and extrapolation region sections of the k_x and k_y integration paths, the pre-extrapolation domain (termed "Region 1" below) refers to the region $(-\xi_1 < k'_x < \xi_1) \cup (-\xi_1 < k'_y < \xi_1)$. Similarly, the extrapolation domain (termed "Region 2" below) refers to the region $(k'_x > \xi_1) \cup (k'_x < -\xi_1) \cup (k'_y > \xi_1) \cup (k'_y < -\xi_1)$. Since one cannot obtain closed-form solutions to the pre-extrapolation and extrapolation domain contributions, reference field values from which one measures accuracy must be chosen; their computation details are provided in Figs. 16 and 17 below.

For the pre-extrapolation domain study, we exhibit the accuracy obtained versus (h) and the Patterson-Gauss quadrature order (p) used to integrate each subinterval. We notice that for both cases, there is the expected increase in accuracy both as one reduces h and increases p .

For the extrapolation domain contribution, we make the typical assumption [19–21] that the integrand is well behaved

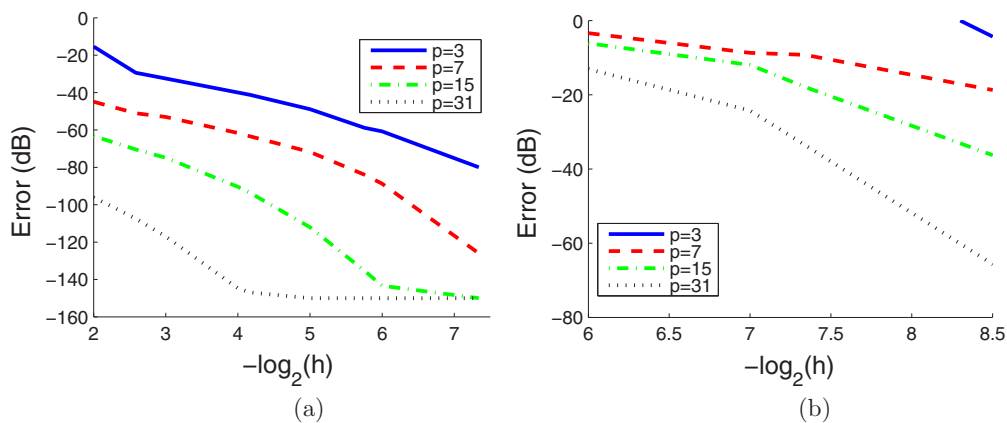


FIG. 16. (Color online) Convergence towards the solution comprising the field contribution from "Region 1". The reference field values are computed using $p = 31$ for both figures, as well as $-\log_2(h) = 9$ for Fig. 16(a) and $-\log_2(h) = 11$ for Fig. 16(b). The reference field values computed for Figs. 16(a) and 16(b) use different h because in the latter scenario, H_z converges more slowly and thus necessitates smaller h values in the nonreference field results to show a meaningful decay in error. As a result, one also requires an even smaller h for the reference field result from which the relative error is computed.

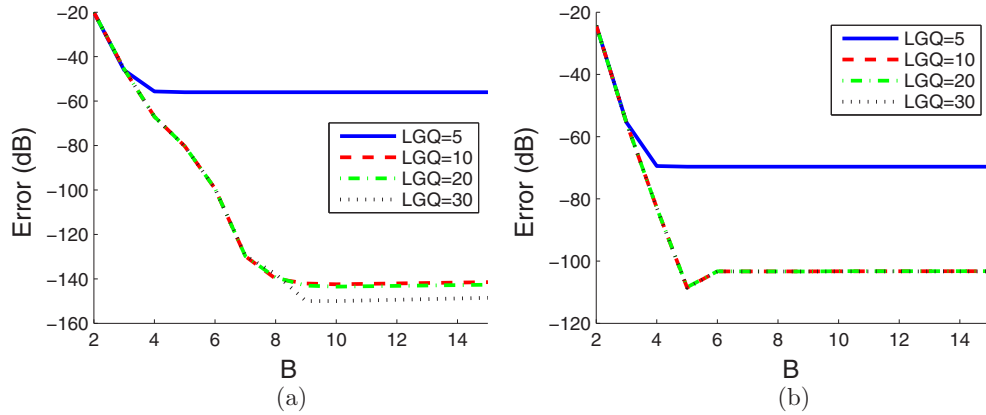


FIG. 17. (Color online) Convergence towards the solution comprising the field contribution from “Region 2”. The reference field values are computed using $LGQ = 30$ for both figures, as well as $B = 150$ for Fig. 17(a) and $B = 1000$ for Fig. 17(b). The reference field values computed for Figs. 17(a) and 17(b) use different B . This is because in the latter scenario, as can be observed, H_z converges more slowly; indeed, while H_z in case two levels off more rapidly than in case one, it fails to reach accuracy near to machine precision within the same range of B exhibited for both cases. Thus similar reasoning applies as that behind using smaller h for the reference and nonreference field results in Fig. 16(b) [versus Fig. 16(a)].

in this portion of the spectral domain and thus do not perform interval subdivision. Instead, we set the k_x and k_y plane extrapolation region interval lengths to be half the spectral period of the Fourier kernels $\exp[ik_x(x - x')]$ and $\exp[ik_y(y - y')]$ (respectively), as suggested in Ref. [20], and examine the variation of accuracy versus the number of extrapolation region intervals employed (B) and the Legendre-Gauss quadrature order used (LGQ) to integrate each interval.²⁷ For the extrapolation domain field contribution, we notice that as one increases LGQ and B there is the expected decay in error. In particular, for small B ($B \sim 3$ for both cases) we notice that tail integral truncation effects dominate the region two error. On the other hand, after a certain value of B ($B \sim 10$ for case 1 and $B \sim 6$ for case 2), we find that aliasing (i.e., inadequate sampling) effects dominate the error.

Note that for Figs. 16–17, errors below -150 dB were coerced to equal -150 dB. This is because error levels below approximately -150 dB do not represent error levels attained due to the convergence characteristic of the formulation itself, but instead represent instances wherein the given and reference answers are equal in all the digits available using finite, double-precision arithmetic.

²⁷ B intervals are used in both the $k'_x > 0$ and $k'_x < 0$ integration path half tails; the same applies for the k_y path half tails.

VII. CONCLUSION

We have presented a general-purpose and efficient pseudo-analytical formulation to compute electromagnetic fields from dipole sources in planar-stratified environments with arbitrary anisotropy, loss, and $\mathbf{r} - \mathbf{r}'$ geometries. The formulation is based on embedding spectral Green’s function kernels within Fourier-type integrals to compute the space-domain fields. Some of the salient features that are combined here to yield a robust algorithm are: (a) judicious selection of a numerically robust integration path, (b) recasting of critical formulas to facilitate accurate field computations and obviate numerical overflow, (c) adaptive integration along the pre-extrapolation region of the integrals, and (d) adaptive extension of the original MMA, applied to environments containing media with anisotropy and loss, both to accelerate the tail integral’s convergence and to endow error control to its evaluation. The formulation’s accuracy has been validated through four sets of numerical data and its convergence properties characterized.

ACKNOWLEDGMENTS

We thank Halliburton Energy Services for the permission to publish this work. In particular, the authors would like to thank Dr. Paul Rodney for his review and comment on this paper.

- [1] B. Wei, T. Wang, and Y. Wang, *Chin. J. Geophys.* **52**, 1350 (2009).
- [2] B. I. Anderson, T. D. Barber, and S. C. Gianzero, in *SPWLA 39th Annual Logging Symposium* (Society of Petrophysicists and Well-Log Analysts, Gulf Freeway, 1998), pp. 1–14.
- [3] A. Howard Jr., *IEEE Trans. Antennas Propag.* **48**, 1376 (2000).
- [4] M. S. Zhdanov, W. D. Kennedy, and E. Peksen, *Petrophysics* **42**, 588 (2001).
- [5] H. Wang, H. Tao, J. Yao, G. Chen, and S. Yang, *Chin. J. Geophys.* **51**, 1110 (2008).
- [6] J. Moran and S. Gianzero, *Geophysics* **44**, 1266 (1979).
- [7] Y. Tang, T. Wang, and R. Liu, in *Annual Meeting* (Society of Exploration Geophysicists, San Antonio, 2007), pp. 678–682.
- [8] M. Jehle, M. Ruegg, L. Zuberbuhler, D. Small, and E. Meier, *IEEE Trans. Geosci. Rem. Sens.* **47**, 1512 (2009).

- [9] S. Lambot, E. Slob, and H. Vereecken, *Geophys. Res. Lett.* **34** (2007).
- [10] S. Lambot, E. C. Slob, M. Vanclooster, and H. Vereecken, *Geophys. Res. Lett.* **33**, 1 (2006).
- [11] M. Jain, J. K. Lotsberg, and J. J. Stamnes, *J. Opt. A: Pure and Applied Optics* **8**, 709 (2006).
- [12] D. Pozar and V. Sanchez, *Electron. Lett.* **24**, 729 (1988).
- [13] D. M. Pozar, *IEEE Trans. Antennas Propag.* **35**, 613 (1987).
- [14] J. R. Mosig and F. E. Gardiol, *Adv. Electron. Electron. Phys.* **59**, 139 (1982).
- [15] M. Paulus, P. Gay-Balmaz, and O. J. F. Martin, *Phys. Rev. E* **62**, 5797 (2000).
- [16] A. Sommerfeld, *Annalen der Physik* **333**, 665 (1909).
- [17] K. Michalski and J. Mosig, *IEEE Trans. Antennas Propag.* **45**, 508 (1997).
- [18] K. Michalski and D. Zheng, *IEEE Trans. Antennas Propag.* **38**, 335 (1990).
- [19] K. A. Michalski, in *Workshop on Integral Techniques for Electromagnetics* (Lausanne, Switzerland, 2007).
- [20] K. A. Michalski, *IEEE Trans. Antennas Propag.* **46**, 1405 (1998).
- [21] J. Mosig, *IEEE Trans. Antennas Propag.* **60**, 2011 (2012).
- [22] R. Niciforovic, A. Polimeridis, and J. Mosig, *IEEE Trans. Antennas Propag.* **59**, 694 (2011).
- [23] A. Alparslan, M. Aksun, and K. Michalski, *IEEE Trans. Microw. Theor. Tech.* **58**, 602 (2010).
- [24] W. C. Chew, *Waves and Fields in Inhomogeneous Media* (Van Nostrand-Reinhold, Hoboken, 1990), Chap. 2, pp. 45–160.
- [25] B. Hu and W. Chew, in *IEEE Antennas and Propagation Society International Symposium 1999* (IEEE, Piscataway, NJ, 1999), Vol. 2, pp. 1182–1185.
- [26] J. R. Mosig, in *Numerical Techniques for Microwave and Millimeter Wave Passive Structures*, edited by T. Itoh (Wiley, New York, 1989), Chap. 3, pp. 133–213.
- [27] A. Caboussat and G. Miers, *Comput. Math. Appl.* **59**, 338 (2010).
- [28] L. B. Felsen and N. Marcuvitz, *Radiation and Scattering of Waves* (IEEE Press, Piscataway, 1994), Chap. 7, pp. 740–820.
- [29] W. C. Chew, *Waves and Fields in Inhomogeneous Media* (Van Nostrand-Reinhold, Hoboken, 1990), Chap. 1, pp. 1–44.
- [30] G. W. Stewart, *Linear Algebra and its Applications* **283**, 151 (1998).
- [31] W. C. Chew, *Waves and Fields in Inhomogeneous Media* (Van Nostrand-Reinhold, Hoboken, 1990), Chap. 7, pp. 375–428.
- [32] MATHEMATICA, Wolfram Research Inc., ver. 8.0.4.0, 2011.
- [33] L. N. Trefethen and D. Bau, *Numerical Linear Algebra* (SIAM: Society for Industrial and Applied Mathematics, Philadelphia, 1997).
- [34] A. S. Kronrod, *Nodes and Weights of Quadrature Formulas, Sixteen-Place Tables* (Consultants Bureau, New York, 1965).
- [35] T. N. L. Patterson, *Am. Math. Soc.* **22**, 847 (1968).
- [36] E. Isaacson and H. B. Keller, *Analysis of Numerical Methods* (Wiley, New York, 1966), Chap. 7, pp. 300–363.
- [37] T. N. L. Patterson, *Commun. ACM* **16**, 694 (1973).
- [38] H. H. Homeier, *J. Comp. Appl. Math.* **122**, 81 (2000).
- [39] J. Kong, L. Tsang, and G. Simmons, *IEEE Trans. Antennas Propag.* **22**, 616 (1974).
- [40] L. C. Chen, *The Log Analyst* **30**, 217 (1989).